Binder-free TiO₂/Carbon Cloth Composite Anode for Electrochemical Energy Storage Devices

by

Ricky Tjandra

A thesis

presented to the University of Waterloo

in fulfillment of the

thesis requirement for the degree of

Master of Applied Science

in

Chemical Engineering – Nanotechnology

Waterloo, Ontario, Canada, 2015

Author's Declaration

I hereby declare that I am the sole author of this thesis. This is a true copy of the thesis including

any required final revisions, as accepted by my examiners.

I understand that my thesis may be made electronically available to the public.

Abstract

Lithium-Ion Capacitors are a new type of hybrid capacitor that combines both supercapacitors and lithium-ion batteries into one device. It has a promising future as the next-generation electrochemical energy storage device for use in applications that require both high energy and power densities such as electric and hybrid electric vehicles. Current commercial lithium-ion capacitors are made up of activated carbon cathodes and graphite anodes. The cathode displays supercapacitative behaviour while the anode is an insertion-type anode commonly used in lithium-ion batteries. Despite being commercialized, many improvements can be made to lithium-ion capacitors especially for the anode such as increasing the power and energy densities.

Anatase TiO_2 has been shown to have excellent performance and a promising candidate to replace graphite as the anode in lithium-ion capacitors. Herein, nanosized TiO_2 has been studied as a binder-free active material as an alternative anode material for lithium ion capacitors. These TiO_2 nanocrystals have crystal sizes smaller than 10 nm and can be dissolved directly into organic solvents, removing the need for any binders or additional materials to improve dispersion on the substrate. The nanocrystals are drop casted onto carbon fiber cloth, forming a composite electrode that is binder-free and flexible. electrode was shown to have a reversible capacity of 315 mAh/g and 410 mAh/g at a current density of 100 mA/g and 34 mA/g respectively.

Acknowledgements

Table of Contents

List of Figures

List of Abbreviations, Symbols and Nomenclature

AC: Activated Carbon

BSE: Back-Scattered Electrons

EDLC: Electric Double Layer Capacitance/Capacitor

EDX: Electron Dispersive X-ray Spectroscopy

EV: Electric Vehicles

FESEM: Field Emission Scanning Electron Microscope

GCD: Galvanostatic Charge and Discharge

HEV: Hybrid Electric Vehicles

LED: Light Emitting Diode

Li-ion: Lithium Ion

LIB: Lithium Ion Battery

LIC: Lithium Ion Capacitor

LTO: Lithium Titanium Oxide

PPy: Polypyrolle

PVDF: Polyvinyldifluoride

SE: Scattered Electrons

SEM: Scanning Electron Microscopy

TGA: Thermogravimetric Analysis

UPS: Uninterruptible Power Supply

XRD: X-Ray Diffractometer

1.0 Introduction

Much attention in the research world has been directed towards the development of electrochemical energy storage technologies with higher power and energy densities [1]–[5]. Such technologies are needed for important applications such as grid-level energy storage, electric and hybrid electric vehicles (EV and HEV) and uninterruptible power sources. Among such technologies, supercapacitors and lithium-ion batteries (LIBs) are the most promising candidates due to their high power and energy densities respectively [1], [3].
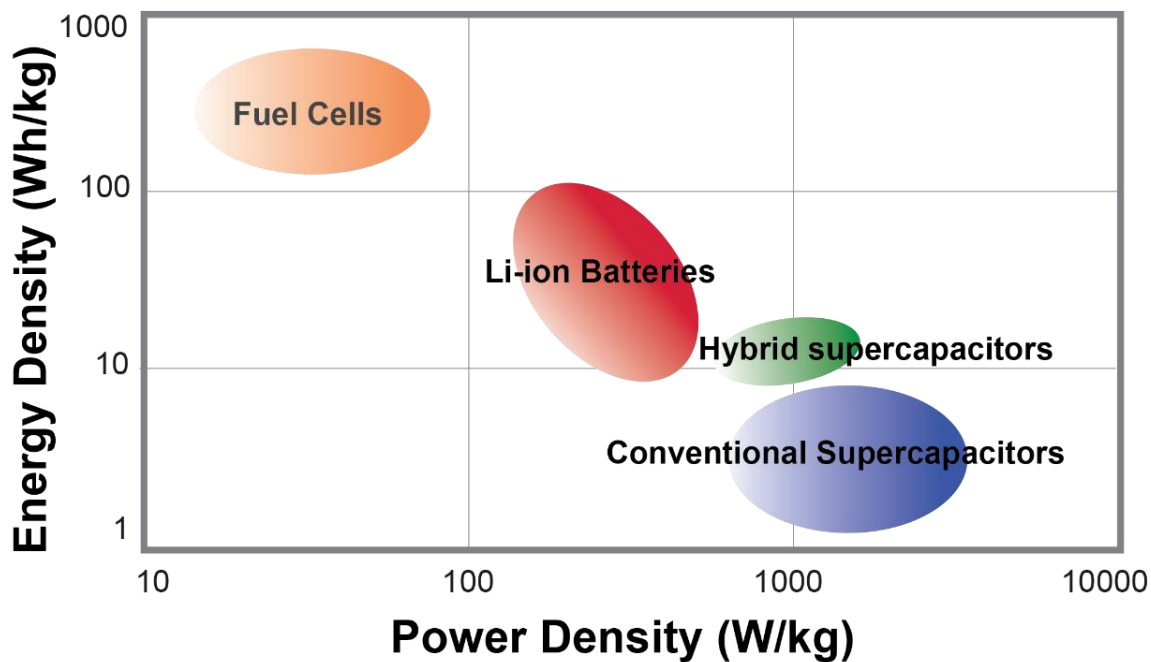
Figure 1 Ragone Plot showing different electrochemical energy devices plotted based on their energy and power densities

For applications such as utility-scale energy storage or HEVs, the energy storage devices need to have both high power and energy densities [6]. Supercapacitors have a distinct disadvantage in which their energy densities are much lower when compared to battery technologies such as lithium-ion. This is a serious drawback that limits the commercialization potential of supercapacitors. Recently, a new class of supercapacitors, dubbed Lithium-Ion Capacitors (LICs) have emerged that combines a lithium-battery anode with a supercapacitative cathode[7]. Due to this marriage of two technologies, LICs have power densities that are greater than traditional LIBs while simultaneously possessing a greater energy density than traditional supercapacitors. LICs are expected to bridge the gap between supercapacitors and LIBs, especially in applications where both energy and power densities are crucial. Another distinct advantage of LICs over LIBs is their longer cycle lives due to the incorporation of the supercapacitative cathode [7].

The overall performance of the LIC depends on two main factors: the energy density of the cathode and the power density of the anode. The overall energy density of the LIC is determined by the cathode because intrinsically, the cathode will always have a lower energy density than the anode. Hence, the cathode is the limiting factor when it comes to energy density. The converse case holds true as well. The limiting factor for the power density is the anode, hence the overall power density of the LIC is determined by the power density of the anode. Current commercially available lithium-ion capacitor uses an activated carbon (AC) cathode and a graphite anode [7]. The graphite anode, although cheap, has slow lithium diffusion kinetics which lowers the device power density. It also suffers from expansion due to lithium-ion

intercalation which lowers its cycle life. Hence, it is important to focus on the anode in order to find a high performance insertion-type anode which is the focus of this thesis.

Commercial LICs are typically assembled by mixing the active materials with polymeric binders and a conductive agent into a slurry which is then pasted onto a metal foil current collector. The polymeric binder is there to improve the contact adhesion between the active material and the current collector while the conductive agent, usually conductive carbon, is there to increase the conductivity of the active material. These additives usually make up to 10-20 weight % of the slurry, decreasing the overall energy and power density of the device. In addition, the heterogeneity of the slurry results in an increased contact resistance and lowers the overall performance of the device. This makes for a compelling case to develop a binder-free electrode [8]–[11]. Hence, it is the direction of this thesis to focus on the development of a high performance, binder-free electrode for use in LICs.

This thesis is structured in way to give the readers a thorough background understanding of recent advances electrochemical storage technologies, specifically LICs. A review of recent advances in the field of anode materials for LICs will then be presented. The work presented hereafter will consist of the development of a novel binder-free composite anode material based on TiO_2 nanocrystals and carbon cloth. This work includes the synthesis, physical characterization and electrochemical characterization of said composite material.

2. 0 Supercapacitors

Supercapacitors were first discovered in 1957 when H. Becker from General Electrics patented a "Low Voltage Electrolytic Capacitor with Porous Carbon Electrodes". Unbeknownst to Becker at the time, the patent was the first mention of an Electric Double Layer Capacitor (EDLC) [12]. At the time, the mechanisms were unknown as the electric double layer phenomena was not yet elucidated. Another version of the EDLC was later invented by the Standard Oil of Ohio (SOHIO) and the technology was later licensed to NEC. NEC introduced EDLCs to the market in 1971 for the purpose of providing backup power for computer memory. A separate breakthrough was pioneered by Brian Evans Conway, who conducted experiments with RuO2, which is a pseudocapacitative material. His research elucidated pseudocapacitance which has a completely difference mechanism compared to Electric Double Layer Capacitance (also abbreviated as EDLC). Over the next 30 years, supercapacitors would experience an explosive market growth when companies such as Maxwell, ELNA and Panasonic entered the fray in commercialization and development of supercapacitors.

2.1 Electric Double Layer- and Pseudo-Capacitors

Supercapacitors can be categorized into 2 main types based on their working principles: electric double layer capacitance (also abbreviated as EDLC) and pseudocapacitance. EDLC stores charge through the reversible accumulation of charged species on the surface of the electrode when a potential is applied, as shown in figure 2. During charging, the negative ions in the electrolyte will be attracted to the positive electrode while the positive ions will be attracted to the negative ions. These ions will form a Helmholtz double layer on the surface of the electrodes and no charge transfer between the ions and the electrodes occur. Since this process does not

rely on mass transport into the electrode, the EDLC can be charged and discharged at a high rate. In addition, the EDLC can be cycled many times ($\sim 10^6$) because it does not require phase changes in the electrode that would otherwise degrade it over time. The EDLC's capacitance can be expressed as [4]:

$$C = \frac{\epsilon_r \epsilon_0 A}{d}$$

Where ε_r is the pemittivity of the electrolyte, ε_0 is the permittivity of vacuum, A is the surface area of the electrode, and d is the thickness of the Helmholtz double layer. From the equation, the capacitance of the EDLC is determined by the specific surface area of the electrodes, the type of electrolyte solution used and the effective thickness of the Helmholtz double layer. The surface area that contributes to the capacitance is only the surface area of the electrode that is accessible to the electrolyte [13]. Thus, it is important to engineer the electrode's surface in order for it to exhibit the right pore structure, pore size and morphology to facilitate surface adsorption of the electrolyte ions.
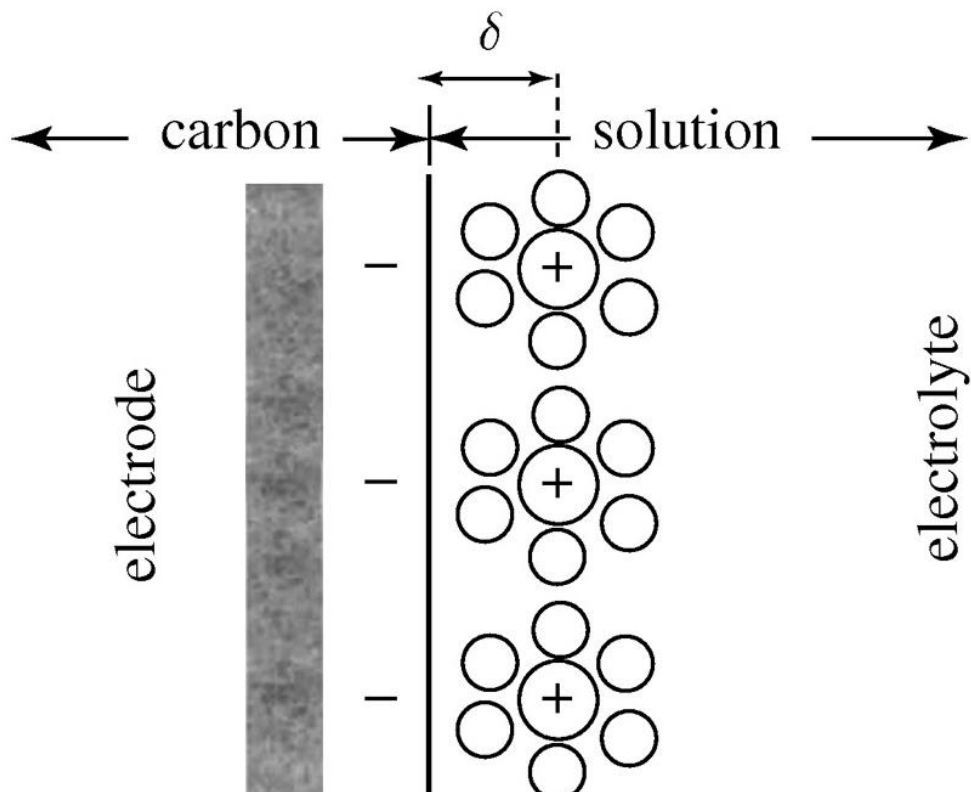
Figure 2 Schematic illustration of electric-double layer capacitance [14]

Pseudocapacitors have completely different charge storage mechanisms when compared to EDLCs. Pseudocapacitors store charge by fast-Faradaic reactions that occur on and a few nanometers under the surface of the active material [3]. These fast-Faradaic reations can be categorized into 3 distinct categories (shown schematically in figure 3): underpotential deposition, redox, and intercalation. Underpotential deposition occurs when there is a more favorable interaction between a substrate and a species compared to the interaction between the species itself. The term underpotential stems from the fact that the electrodeposition of the species onto the substrate is lower (less negative) than the Nersnt potential for reducing said species. Redox pseudocapacitance occurs when a charged species is adsorbed onto or near the surface of an active material and a Faradaic charge transfer occurs. Intercalation

6

pseudocapacitance occurs when a charged species intercalates into the crystalline layers of an active material and a charge transfer reaction occurs without a corresponding phase change. The pseudocapacitance of a material can be defined as [3]:

$$C = \frac{(nF)X}{mE}$$

Whereby n is the number of electrons transferred, F is Faraday's constant, X is the fraction of the surface or inner structure covered by the adsorbed species, m is the molecular weight of the active material, and E is the potential. The main advantage of pseudocapacitance versus regular redox and intercalation processes, such as the ones utilized in batteries, are that they occur on or near the surface of the active material. Consequently, the processes are not limited by solid-state diffusion kinetics and can occur at time scales that are shorter than ones in batteries. Similar to EDLCs, pseudocapacitative electrodes need to be engineered to have high electron conductivities and high surface area/porosities to increase the available surface area for the Faradaic reactions. In addition, for intercalation pseudocapacitance, nanostructured electrodes are advantageous due to the fact that only the surface and near surface are used in the energy storage process.

Underpotential Deposition	Redox Pseudocapacitance	Intercalation Pseudocapacitance
$Au + xPb^{2+} + 2xe^- \rightarrow Au \cdot xPb_{ads}$	$RuO_x(OH)_y + \delta H^+ + \delta e^- \leftrightarrow RuO_{x-\delta}(OH)_{y+\delta}$	$Nb_2O_5 + xLi^+ + xe^- \leftrightarrow Li_xNb_2O_5$
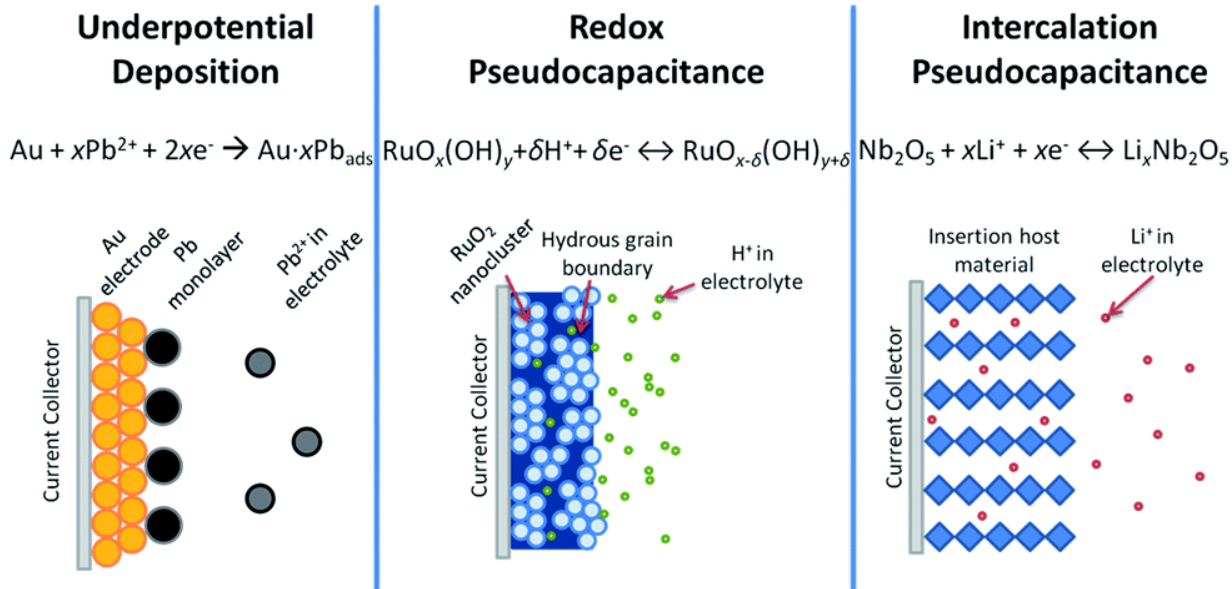
Figure 3 Schematic illustration of pseudo-capacitance [3]

2.2 Lithium-Ion Capacitors

Lithium-ion capacitors are a relatively new development which combines EDLCs with LIBs. Specifically, lithium-ion capacitors utilize an EDLC cathode and an insertion-type electrode that is used in LIBs with a non-aqueous electrolyte [15]. Lithium-ion capacitors have several distinct advantages when compared to both supercapacitors and LIBs. First, LICs are more energy dense than regular supercapacitors due to the insertion-type anodes which can store a greater amount of energy compared to both double-layer capacitance and pseudocapacitance. Second, LICs are more power dense compared to LIBs due to its EDLC cathode, which does not rely on kinetically slow reactions. Third, LICs have cycle lives that are much greater than LIBs and are comparable to supercapacitors [7], [15], [16]. These properties make LICs very attractive for applications that demand both high energy and power densities such as HEVs. A schematic illustration of the charge storage mechanism for lithium-ion capacitors is shown in figure 4.
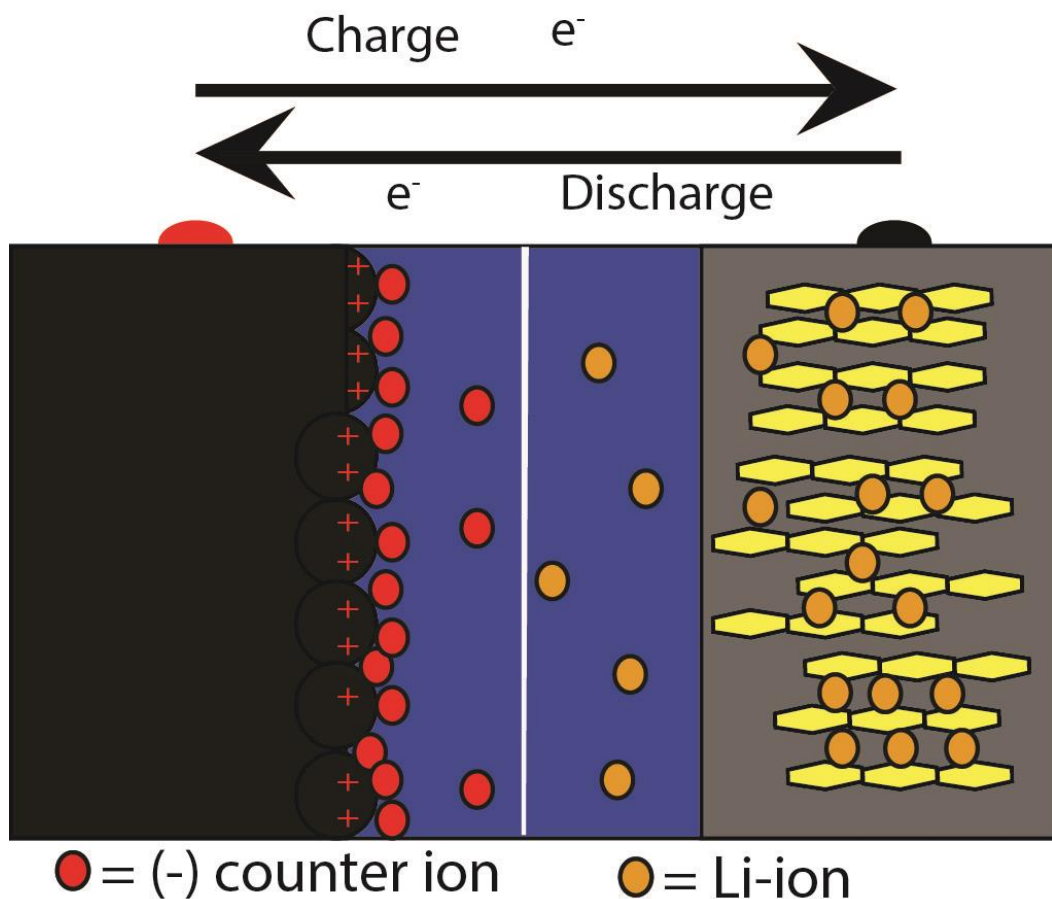
Figure 4 Charge storage mechanisms of a lithium-ion capacitor

A typical LIC design contains an EDLC cathode, an anode that is pre-doped with lithium, a separator, electrolyte, and a housing to contain all of the aforementioned parts. Commercial LICs use activated carbon as cathodes and graphite as anodes. Typically, the electrolyte used is similar to ones used in LIBs, i.e. 1M LiPF6 in 1:1 mixture of ethyl carbonate (EC) and dimethyl carbonate (DMC), though diethyl carbonate (DEC) is also sometimes used instead of DMC. The separator is usually a polymer such as polypropylene. During discharge, the PF_6 anions will be attracted to the positive electrode and form a Helmholtz double-layer on the surface of the

electrode. Conversely, the lithium-ions will intercalate into the structure of the anode. During discharge, the reverse reactions will occur. The half-cell reaction for graphite can be expressed as [7]:

$$xLi^+ + x\,e^- + xC_6 \leftrightarrows xLiC_6$$
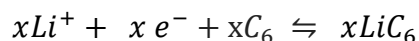
A perfect graphite lattice can accommodate x moles of lithium ions for every six moles of carbon atoms which corresponds to a theoretical specific capacity of 372 mAh/g when x is equal to 1 [7], [17], [18]. Figure 5 shows a typical galvanostatic charge and discharge curve of a graphite half-cell.
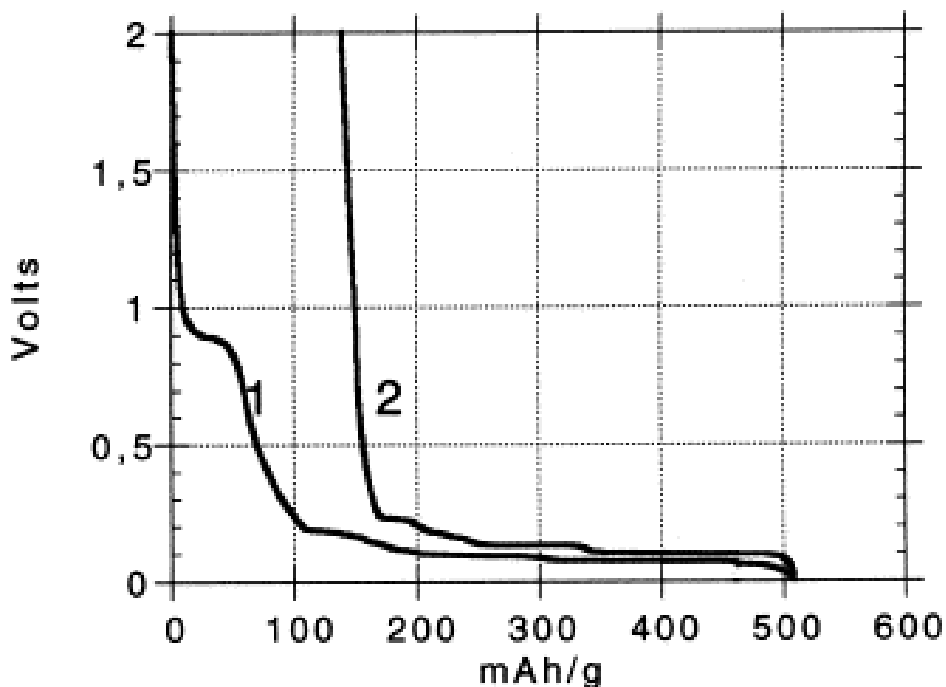
Figure 5 First charge and discharge curves of a graphite half-cell [1]

A voltage plateau around 0.8-0.9 V occurs in the first discharge cycle of the graphite electrode due to the formation of a solid electrolyte interphase (SEI) which causes an irreversible loss of capacity. This phase is a passivating layer resulting from the irreversible reaction between the electrode and the electrolyte. As the potential of the graphite electrode goes closer and closer to the potential of lithium metal, a number of distinct plateaus below 0.3V is observed. These plateaus can be attributed to the insertion of lithium into the graphite structure. The insertion happens in stages, denoted as n, which correspond to the number of graphene layers in-between two successive intercalated layers. The composition of these stages are well-studied and are as follows: stage-1 (LiC_6), stage-2 (LiC_{12}), stage-3 (LiC_{25}-LiC_{30}), stage-4 (LiC_{44}-LiC_{50})[1]. The stating process during intercalation/de-intercalation is a thermodynamically driven process that is dependent on the energy it takes to widen the gap between graphene layers to accommodate lithium-ions.

Unlike graphite, the activated carbon cathode will display a linear behaviour without any plateaus due to its EDLC behaviour. Consequently, the cathode will have a much smaller specific capacity compared to the anode. This capacity inequality means that the masses of the cathode and anode must be controlled and optimized for to obtain a device that has the best performance. LIC cathodes utilize high specific surface area materials that exhibits EDLC. To date, the best materials to be used for this purpose are carbonaceous materials such as activated carbon. Activated carbon is currently used as a cathode material in commercial LICs. Activated carbon is an umbrella term designated to carbon materials that have undergone treatment in order to increase its specific surface area by introducing micro- and mesopores into their structures. There are a great variety of activated carbons with different properties based on the precursor materials

and the activation process. Currently, biomass (peanut shells, coconut shells etc.) are the most popular choice for AC precursors due to its cost and wide availability.

Although graphite is currently used as the anode material in LICs, several improvements can be made. For one, graphite's lithium-insertion potential is low which makes it prone to side reactions and thermal runaway reactions. Second, the diffusion kinetics of lithium into the graphite matrix is sluggish, making it difficult for it to be charged and discharged quickly. Finally, graphite experiences a large volume change when lithium is inserted into its structure which causes degradation and reduces the cycle life of the electrode [19]. Thus, there is a need to find a new insertion-type electrode for use in LICs.

Several criteria need to be considered when discussing insertion-type electrodes:

    i)   The organic electrolytes (carbonate based) that are conventionally used in LIBs and LICs are stable between 1-4.5 V vs Li/Li^+ [20]. At potentials outside of this window, the electrolyte will be oxidized and/or reduced, which results in the irreversible consumption of lithium ions [20]. Hence, it is important to find an electrode that is has a redox potential that matches the electrolytes'

    ii)   The cathode material in LICs can exhibit cycling lives that are on the order of 10^6 cycles. Thus far, reported insertion-type electrodes only have cycling lives that are at least 2 orders of magnitude smaller than those of the cathode materials [19]. Hence, it is important to consider the cyclability of the anode material because it is the limiting factor of the final cell's cyclability

iii)   The conductivity of the anode material needs to be considered due to the effect it has on the rate performance, i.e. the speed in which the cell can be charged and discharged. A high conductivity material will have a better rate performance than a lower one [19].

Based on these criteria, TiO_2 and its polymorphs/compounds have a promising future for use in LICs for reasons discussed hereafter.

3.0 TiO₂ based Electrode materials

3.1 TiO₂ Polymorphs

TiO_2 based compounds and its polymorphs have been recently investigated as an active material for use in both LIBs and lithium-ion capacitors. TiO_2 is attractive due to its abundance, low-cost and environmental friendliness. The intercalation/de-intercalation reaction of lithium-ions into the structures of the TiO_2 polymorphs can be expressed as the following [16], [19], [21]:

$$xLi^+ + TiO_2 + x\,e^- \leftrightharpoons Li_xTiO_2$$
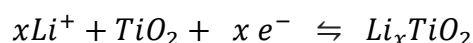
The number of moles of lithium (between 0 and 1) that can be inserted varies with the different polymorphs, their nanostructures and crystalline size. However, the intercalation/de-intercalation occurs roughly around 1.5-1.8V vs Li/Li⁺ for all of the different TiO_2 polymorphs [22]. This high redox potential boosts the safety of TiO_2 –based electrodes because it avoids most electrolyte side reactions that occur at lower potentials. However, the low Li⁺ diffusivity and electron conductivity of bulk TiO_2 severely limits its potential as an anode material. Different strategies of varying success have been employed in order to improve the ion and electron conductivities of TiO_2. The easiest and most popular way to improve lithium-insertion into TiO_2 is to design and synthesize different nanostructured TiO_2 [19], [22].
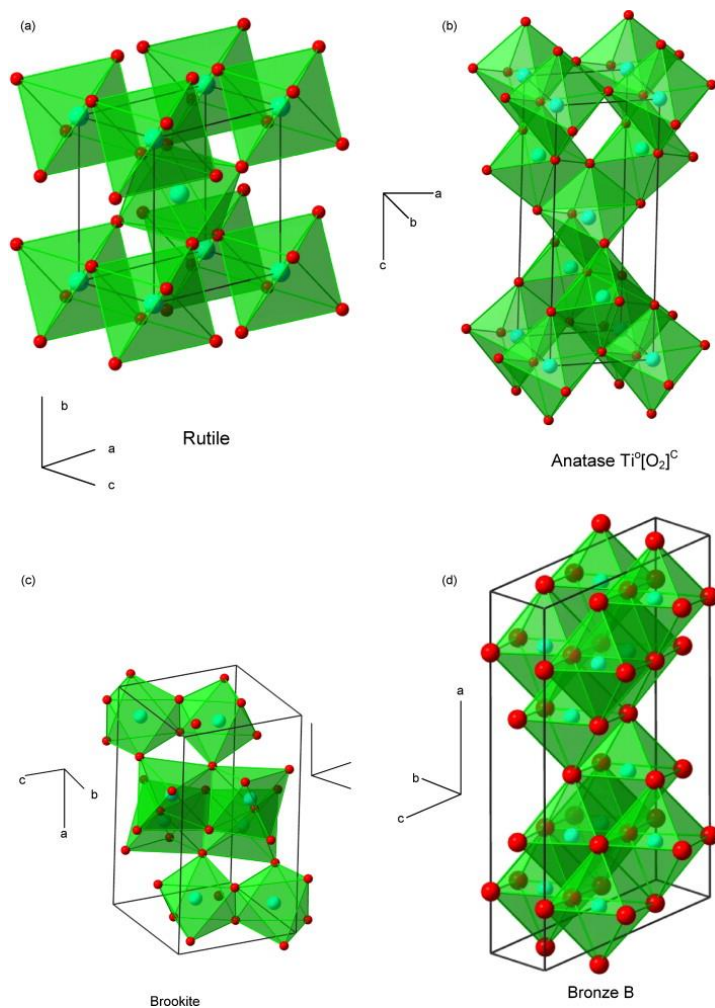
Figure 6 Crystal structures of TiO₂ polymorphs [20]

3.1.1 Rutile TiO$_2$

Rutile TiO$_2$ is the most thermodynamically stable of all the TiO$_2$ polymorphs and is a closely packed structure consisting of TiO$_6$ octahedra that share edges and corners at the c-axis and ab-planes respectively [22], [23]. It also has the lowest lithium storage capabilities in its bulk form [22]. One reason for the low lithium storage capability is the anisotropic behaviour of Li$^+$ into the crystal structure of rutile TiO$_2$. The Li$^+$ diffusion coefficient along the c-axis is approximately 10^{-6}cm^{2}s^{-1} compared to 10^{-15}cm^{2}s^{-1} along the ab-plane at room temperatures [24], [25]. This

anisotropic reaction alongside with the repulsive interaction between Li^+ pairs in the c-axis and ab-planes restrict the insertion of li-ions into bulk rutile TiO_2 well below its theoretical capacity [24], [25].

To combat this low-capacity, many different nanostructures of TiO_2 has been investigated. Hu et al. [6] showed that li-ion insertion into rutile TiO_2 increases as the size decreases. They synthesized rutile nano-needles with a dimension of 10x40nm and reported that the up to 0.5 mol of Li per mol of TiO_2 can be reversibly reacted. This is a significant improvement when compared to micron-sized particles that only managed a small degree of lithium-insertion (up to 0.25 mol) [26]. Reddy et al [27] used a facile hydrothermal sol-gel method to synthesize nanocrystalline rutile TiO_2. They showed that insertions of up to 1 mol of Li per mol of rutile TiO_2 was possible using standard conditions.

3.1.2 Anatase TiO_2

Anatase TiO_2 is comprised of TiO_6 octahedra that form planar chains due to the sharing of adjacent edges between 2 octahedra [23], [28]. The capacity of Li^+ diffusion into bulk anatase TiO_2 is much higher compared to rutile TiO_2, allowing up to 0.5 mols of Li^+ per mol of TiO_2[9]–[12]. That being said, the lithium-insertion can be improved by reducing the particle size and introducing various nanostructures, similar to the strategy employed for rutile TiO_2 [9], [10], [11].

Wagemaker et al [21] studied the impact of particle size in the lithium-insertion reaction of anatase TiO_2. They found that the crystalline domain size is a crucial parameter for the

thermodynamics and kinetics of intercalation reactions. Figure 7 shows the phase diagram of Li in anatase TiO_2 studied by Wagemaker that shows the extent of Li^+ intercalation versus different particle sizes. They discovered that at higher particle sizes, the extent of Li^+ insertion into the crystal structure is kinetically limited. An interesting phenomena occurs when the crystal sizes go below 10 nm where the behaviour of the Li_xTiO_2 resembles a solid solution [21]. Chen et al [9] reported TiO_2 nanocrystals that were composited with carbon nanotubes that achieved an excellent high rate performance (almost 150 mAh/g at 10C). These anatase TIO_2 particles were synthesized using a solvothermal method and have a monodispersed particle size distribution of around 6 nm. The addition of the carbon nanotubes allowed for the formation of an electron-conductive network that overcomes the inherently poor electronic conductivity of TiO_2 [9].
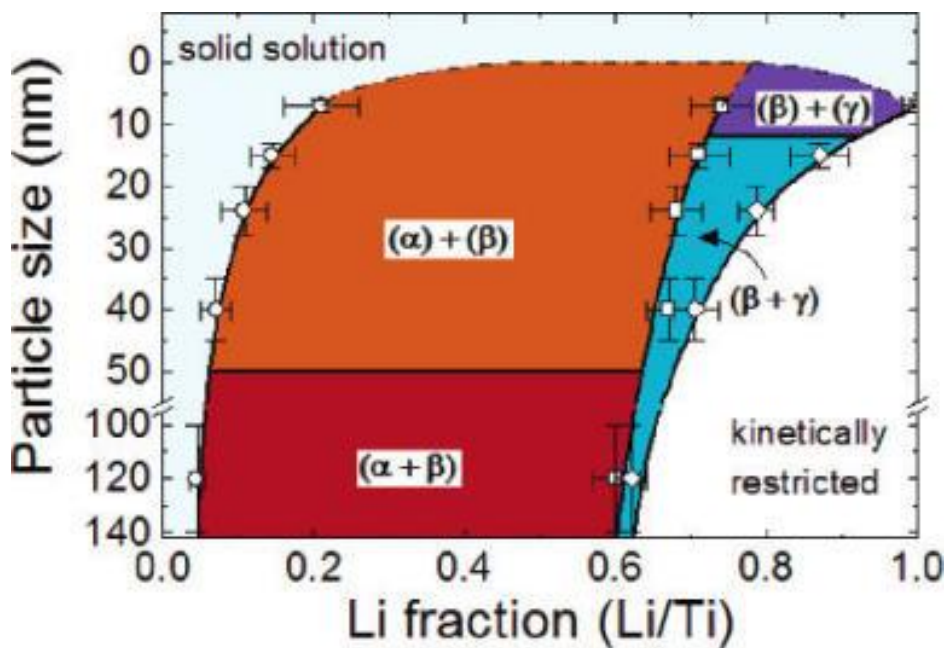
Figure 7 Phase diagram of lithium insertion into anatase TiO₂ [27

3.1.3 Other TiO₂ Polymorphs

In addition to anatase and rutile, Brookite and Bronze are two other meta-stable polymorphs of TiO_2. Bronze TiO_2 has a perovskite-like open structure composed of TiO_6 octahedra [30] while Brookite TiO_2 forms an orthorhombic structure due to the sharing of 3 edges between adjacent TiO_6 octahedra [23].

Similar to rutile TiO_2, brookite TiO_2 has a low Li-insertion fraction (x = 0.03 to 0.3) in the bulk phase. However, Reddy et al [31] showed that, similar to rutile, the insertion of Li^+ into brookite shows a very strong size dependency. Their group proved that a Li^+ insertion fraction of up to 0.9 was possible using nanocrystalline brookite TiO_2 as the crystal size approaches 10 nm (shown in Figure 8).
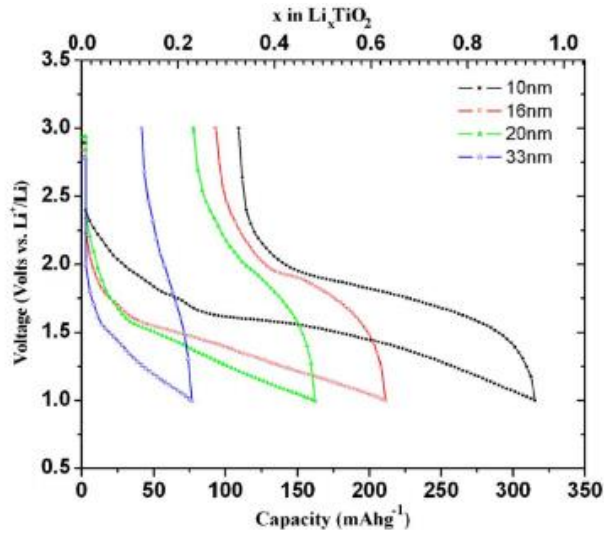
Figure 8 Size depency of lithium insertion extent into brookite TiO [30]

Bronze TiO_2 exhibits a different and unique Li-insertion mechanism compared to other polymorphs of TiO_2. Zukalova et al [32] showed that bronze TiO_2 exhibits pseudocapacitive

behaviour and is not limited by the Li^+ diffusion into the crystalline matrix but by a pseudocapacitative surface fast-Faradaic reaction.

3.1.4 Lithium Titanate (LTO)

Lithium titanates have been investigated as insertion-type electrodes since the early 1990s. Lithium titanates are oxides with spinel structures that have the formula $Li_{1+x}Ti_{2-x}O_4$ where $0 \leq x \leq 1/3$ [33], [34]. Lithium titanates are an attractive option for insertion-type electrodes due to their minimal structural expansion even after full lithiation (zero-strain material) [34]. This property allows them to be charged/discharged at a high rate for a large number of cycles without much material degradation. Similar to TiO_2, LTO has a high Li^+ insertion potential ranging from 1.36V to 1.56V vs Li/Li^+ [35] which helps avoid any side reactions. In addition, there has been no known side reactions between LTO and its electrolytes that can contribute to any irreversible loss of capacity[22]. On the other hand, compared to TiO_2 and its polymorphs, lithium titanates have a theoretical maximum capacity of only 150 mAh/g [22], [36], [37]. Currently, nanostructured LTO are being used to in commercial li-ion batteries for large-scale applications.

3.1.5 TiO_2 Composites

Besides the reduction of TiO_2 particle size and introducing nanostructures, compositing TiO_2 polymorphs with other complimentary compounds have been effective at increasing the electrochemical performance of TiO_2. Since TiO_2 has poor electron conductivity, it has been a popular strategy to combine it with materials that have excellent conductivities such as carbon black, graphene, and carbon nanotubes.

Chen et al [9], [38] utilized nanocrystalline anatase TiO_2 that is composited with carbon nanotubes in order to form a free-standing electrode for use in supercapacitors. The carbon nanotubes form a connective and conductive network that helps improve the sluggish electron transport in TiO_2. The intimate contact between carbon nanotubes and TiO_2 allows for greater lithium-insertion compared to other TiO_2 morphologies and composites as shown in figure 9.
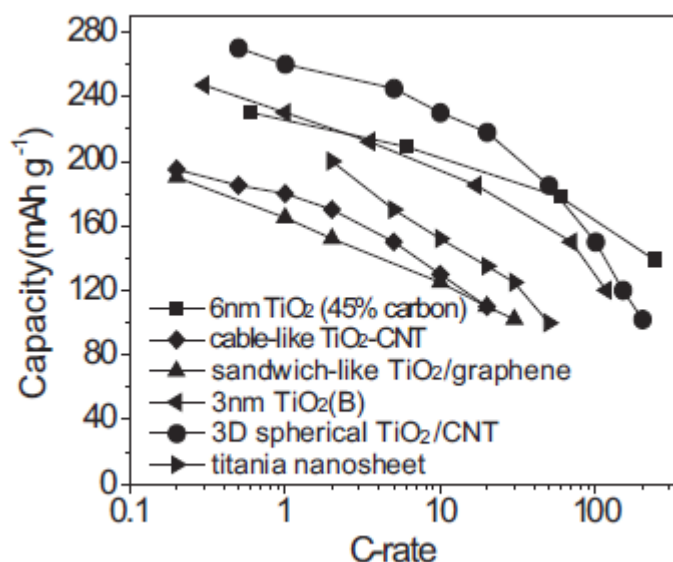
Figure 9 Rate capability comparison between various reported TiO₂ morphologies [9]

Balogun et al [39] utilized a composite of TiO_2 and TiN nanowires that were grown on carbon cloth as a flexible anode for LIBs. The resulting composite had an excellent rate performance, having a discharge capacity of 136 mAh/g at 30C. In addition, the composite was made into a flexible lithium-ion battery with a $LiCoO_2$ cathode and had a discharge capacity of 222 mAh/g at a 90° bending state. Jiang et al [40] synthesized TiO_2/graphene/polypyrolle (PPy) composite films that were used as an electrode in an asymmetric supercapacitor device. The resulting film, shown in figure 10, are both flexible and robust enough to be handled by hand.
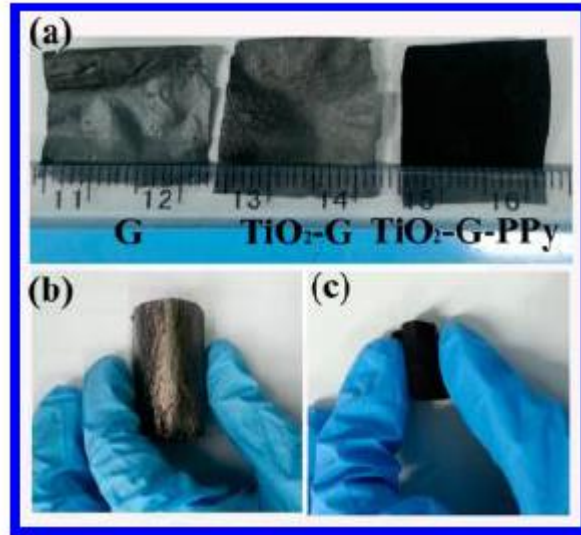
Figure 10 Flexible TiO₂/Graphene/PPy composite film [39]

4.0 Physical and Electrochemical Characterization

Physical characterization techniques are an integral part in materials research. It is helpful to elucidate the mechanisms behind a material's apparent properties and help shape the direction of the research. Characterization is also helpful in determining and confirming the results of a particular experiment. For example, Scanning Electron Microscopy (SEM) can determine the morphology of a newly synthesized material and can provide rough estimates of particle size. In addition, it can also be used to determine material composition through the use of Energy Dispersive X-ray Spectroscopy (EDX) or back-scattered electrons (BSE).

Electrochemical characterization techniques are also important when doing research in the field of electrochemical storage devices. It can help determine a whole suite of important parameters such as capacitance, energy and power density.

Both physical and electrochemical characterizations techniques used in this thesis will be explained in detail in the coming section.

4.1 SEM

SEM is a very valuable microscopic technique, without which it would be impossible to discern the shape and morphology of nano-scaled objects. A top-of-the-line SEM can resolve images of below 1 nm, which is orders of magnitude greater than the resolution of the best optical microscopes [41]. Unlike traditional light microscopes, SEM uses electrons instead of visible light as a probe. Electrons have a DeBroglie wave length orders of magnitude smaller than photons which makes the resolution limit of the SEM much greater than that of an optical

microscope. The primary advantage of the SEM is the fact that it has great resolution while requiring minimal sample preparation. It is also considered non-destructive for the most part. Finally, data can be gathered fairly quickly using the SEM because of its simple setup and operation. The main disadvantage of SEM is that it can only probe the surface of the samples. Any information regarding the structure below the sample surface are lost.
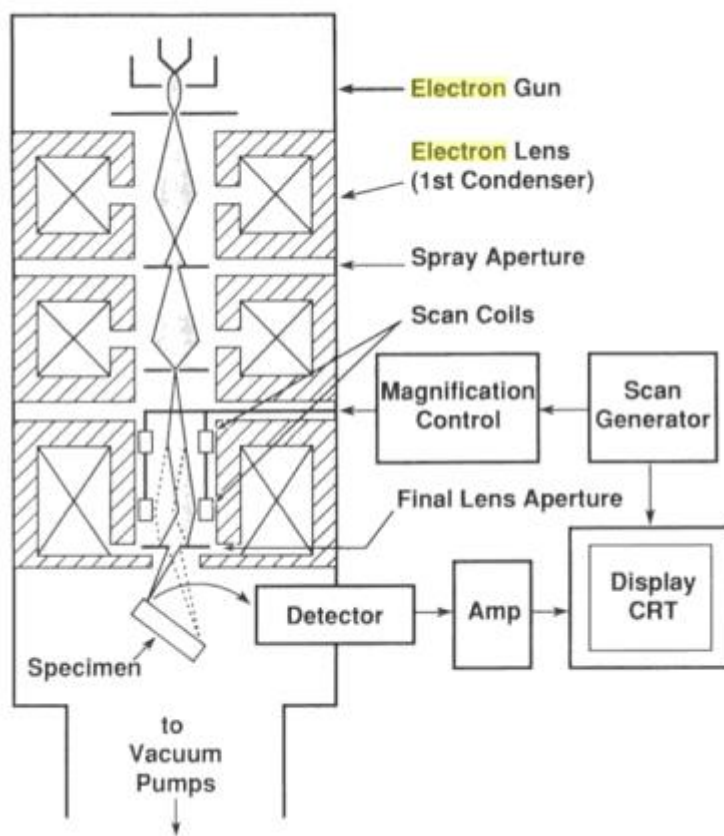
Figure 11 Schematic illustration of typical SEM setup [42]

A typical SEM consists of an electron gun, electromagnetic focusing lenses, and movable sample stage and electron detectors. Some SEMs also have optional x-ray detectors for EDX mapping.

Most SEMs operate in a moderately high vacuum (~10^{-5}-10^{-6} torr) although there are SEMs that are purpose-built for operation in a low vacuum and/or wet conditions [41].

SEMs operate by shooting a high energy electron beam at the sample. These electrons will lose their energy as they interact with the electrons present in the sample. These interactions present themselves as BSE, secondary electrons (SE), photons in the form of x-rays, visible light and heat. Most of these interactions can be captured using specialized detectors and can be interpreted to elucidate different properties of the sample.

SEs are low energy electrons (<50 eV) that are ejected from the sample when due to inelastic collisions that occur with the electron beam generated from the gun. These electrons typically come from the surface (few nanometers) of the sample and are useful in determining topographical and morphological information. The SE mode is one of the most commonly used modes of the SEM.

BSE are high energy electrons that are originally emitted by the electron gun but are back-scattered due to elastic collisions with the sample's electron cloud. BSEs can be used to rapidly determine the phase composition of a material. Since elements with high atomic numbers have a denser electron cloud, more electrons tend to be back-scattered which results in a stronger signal and a brighter image. Conversely, elements with lower atomic numbers will back-scatter less and will present a weaker signal and a darker image.

Typical sample preparation include:

1. Drying in a vacuum oven especially if the sample is prone to outgassing

2. Coating with a conductive material, typically gold, if the sample is non-conductive

Samples are placed onto an SEM "stub" using a piece of conductive carbon tape. The sample stub can then be placed onto the sample stage and be imaged.

4.2 X-Ray Diffraction

X-Ray Diffraction (XRD) is an analytic technique which can determine the crystal structure of an unknown material, the orientation of a crystal and measure the spacings between layers of atoms. It can also measure the size, shape and internal stresses of a crystalline region. The graph that is obtained from the XRD machine is called an x-ray diffractogram which shows the intensity of scattering of the x-ray at different angles.

XRD is not a standalone technique - that is, in absence of other information, XRD cannot be used to determine an unknown sample since it only determines the crystal structure of a material. For example, if one were to provide 2 samples of varying composition but possessing identical crystal structures, XRD would not be able to distinguish between them. In order to correctly identify the composition of a structure, one would have to compare the diffractograms of an unknown samples with ones that have been previously catalogued. Fortunately, the International Centre for Diffraction data (ICDD), formerly called the Joint Committee on Powder Diffraction Standards (JCPDS), keeps a database of all known diffractograms to allow for the identification of unknown materials.

XRD is typically considered a non-destructive characterization method. It is also a rapid characterization method with minimal sample preparation and can provide unambiguous, easy to interpret results. However, the downsides of XRD is that a reference is needed to identify a particular sample and that there is a minimum sample amount that is required.

A typical x-ray setup requires 3 basic elements: an x-ray tube, a sample holder and an x-ray detector. The x-ray tube generates the x-rays by blasting a target material, most commonly copper, with high energy electrons. The target material will then produce a characteristic x-ray spectra that can be filtered using monochromators to obtain a single wavelength (1.54 A for copper). The monochromated x-rays are then collimated and then shot at the sample stage and any scattered rays are captured by a detector.

Figure 12 Benchtop XRD unit

The interaction of the incident x-rays with the sample will produce a diffracted x-ray beam that will interfere constructively and destructively with itself when the conditions of the Bragg equation is satisfied. The Bragg equation is:

$$n\lambda = 2d\sin\theta$$

The Bragg equation relates the wavelength of incident x-rays to the angle of incidence and the spacing between crystal planes. In order to produce a spectra of diffracted rays to construct the diffractograms, a goniometer is used to rotate the sample holder at θ while the x-ray detector is rotated at 2θ. The Bragg equation can be used to determine the spacing between the crystal planes of a sample which is useful to elucidate the crystalline structure of a sample. Sample identification can also be done by comparing the sample diffractogram with a database of known crystalline samples. In addition, the size of crystalline domains of a (nano-scaled) sample can be estimated using the Scherrer equation [17]:

$$\tau = \frac{K\lambda}{\beta cos\theta}$$

Where τ is the mean size of the crystalline domains, K is a shape factor (usually close to 1), lambda λ is the incident x-ray wavelength, β is the full width half-max (FWHM) of the crystalline peaks and θ is the Bragg angle where the peak is found. In general, the larger the FWHM, the smaller the crystalline domains are.

XRD sample preparation typically involves the grinding of the sample into fine powder. The ground powder is then distributed evenly onto the sample holder or onto a piece of sticky tape. Samples in the form of thin-films can also be analyzed. In order to avoid interference, the substrate is typically amorphous although post processing can be used to eliminate the substrate from the diffractrogram provided that the substrate material is of a known composition.

4.3 Raman Spectroscopy

Raman spectroscopy is a non-destructive spectroscopic characterization technique that utilizes light scattering in order to quantify and identify a sample. Besides the fact that Raman spectroscopy is non-destructive, it is also useful to identify many inorganic and organic samples and do not require any special sample preparation. It can even work with samples that are in an aqueous solution due to the fact that water is a weak Raman scatterer. The spectra obtained from Raman spectroscopy are very specific and distinct, which allows for fast chemical identification when compared to a known database (similar to XRD). Besides qualitative analysis, Raman spectroscopy can also be used qualitatively because the area of a Raman band is proportional to the concentration of the molecule that caused the scattering.
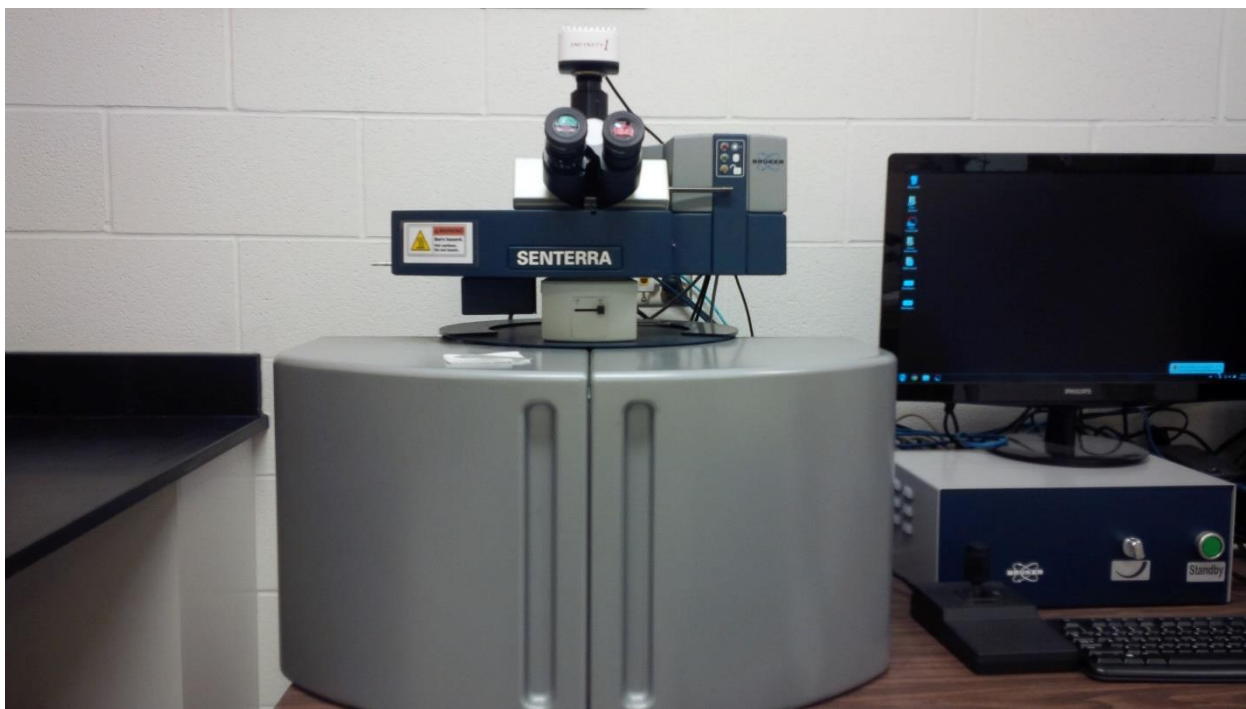
Figure 13 Bench top Raman spectroscope unit

A typical Raman setup consists of an optical microscope, movable sample stage, laser source, laser filters, monochromator and a photodetector. The sample is usually placed on a glass slide and then placed in focus using the optical microscope (which will also serve to focus the laser). Once the sample is focused, the sample chamber is closed to minimize any ambient light from leaking in and the laser is turned on. The photon beam will interact with the electron cloud of the sample and excite it to a virtual state for a brief period of time.
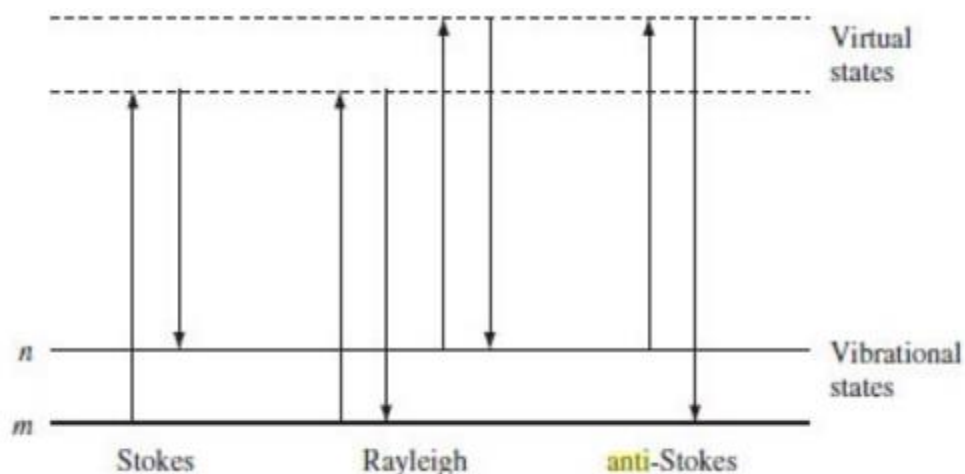
This interaction will create an inelastically scattered photon that will have either a lower or higher frequency than the incident photon (dubbed "Raman scattering". Photons that have a higher frequency than the incident photon are said to have undergone an anti-stokes shift. Conversely, photons that have a lower frequency than the incident are said to have undergone a stokes shift. Only a small amount of photons undergo Raman scattering, most photons that are produced by the incident light undergo elastic scattering where the scattered electron has the same frequency as the incident photons. These types of photons are useless for identification of the samples and are filtered out. The Raman scattered photons are collected based on their frequency shift and then plotted against the intensity in order to form a Raman spectra. These spectra are unique to individual molecules due to the differences in vibrational, rotational and stretching of the bonds of different molecules.

4.4 Thermogravimetric Analysis

Thermogravimetric Analysis (TGA) is a method of characterization in which a sample's physiochemical changes are monitored as a function of increasing temperature or increasing time (at a constant temperature). TGA can provide information on many physical characteristics such as phase transitions and chemical characteristics such as thermal stability. TGA is commonly used to investigate materials' characteristics that exhibit a mass change. Unlike any of the characterization methods explained thus far, TGA is a destructive technique because it requires the samples to be heated often until it decomposes into its constituents.

A typical TGA setup consists of a precision balance, sample pan and a programmable furnace with a high precision thermocouple. In a typical TGA experiment, a sample pan is first placed onto the precision balance so that the computer can record the mass of the empty pan. Then, the sample is loaded onto the pan and heating can begin. Most TGA can conduct experiments in air or other gases, inert and/or reactive. Once heating begins, the TGA machine will continuously monitor and record the mass of the sample and the temperature inside the furnace until a set temperature and/or time is reached. Sample heating rates can vary from very quick (~50˚C/min) to very slow (~1-2˚C/min) depending on the resolution required. For example, finding the onset decomposition of a temperature will require slower heating rates while finding the carbon content of a polymer can be done at greater heating rates. Data processing of the TGA results will usually yield a plot of percentage mass loss versus temperature.

TGA requires little to no sample preparation. The most important step of the sample preparation is to make sure that the sample pan is cleaned thoroughly and is free of any unwanted substances.

TGA can be done with any form of solid or liquid samples and minimal sample masses (>1 mg) are needed.

4.5 Half-Cell Electrochemical Testing

In order to evaluate and compare the performance of the anode material it is necessary to perform a standard array of electrochemical characterization tests. Typically, new electrode materials are screened using half-cell testing. As the name implies, half-cells consists of one half of an electrochemical cell. In the case of a lithium-ion capacitor, the positive electrode half-cell consists of the absorption and desorption of the negative ion in the electrolyte while the negative electrode half-cell consists of the intercalation and de-intercalation of lithium ions in the host anode material. Figure 19 shows a schematic illustration of a lithium-ion capacitor half-cell.
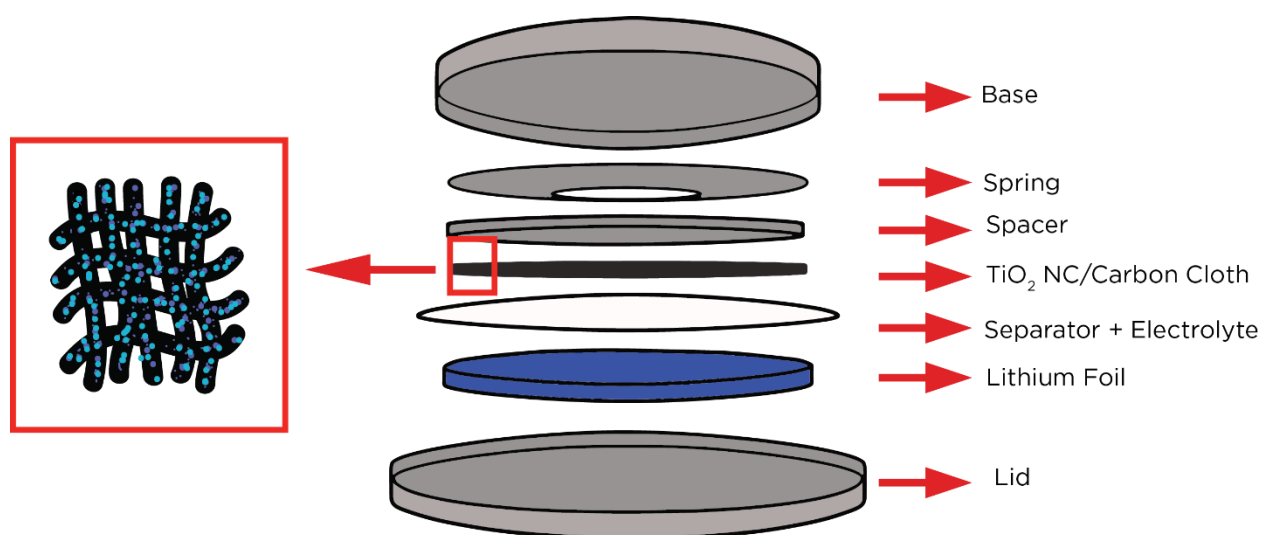
Figure 15 Schematic illustration of a coin half-cell assembly

The first and most important characterization technique is the galvanostatic charge and discharge (GCD). The GCD is a technique that is used to determine a host of important electrochemical

parameters about the anode material such as energy and power density, charge/discharge profiles and also the rate capabilities of the anode which is how fast lithium-ions can intercalate and de-intercalate. GCD is usually done using a battery testing station that has the capability to both draw and provide a constant current (galvanostat).

Figure 16 Neware bench top battery tester unit

In a typical GCD experiment, a cell (either half or full) is charged and discharged to a preset potential at a certain current (the charge and discharge current do not necessarily have to match) for the desired number of cycles. The resulting data can then be processed accordingly depending on which electrochemical characteristic of the material is desired. For example, one can plot the energy capacity of the material versus the charge/discharge current. The resulting plot will illustrate the rate capabilities of the material since as the current increases, the capacity will decay based on several different factors.

5. 0 Synthesis of Binder Free TiO$_2$/Carbon Cloth composite for use in electrochemical energy storage

5.1 Introduction and Project Purpose

LIBs are electrochemical energy storage devices that rely on materials that are able to store lithium-ions in their crystalline matrix structures. Its use is wildly prevalent in today's society due to its portability and high energy densities. However, for certain applications that require a high power density, LIBs are still not quite up to the challenge. On the other hand, supercapacitors are devices that rely on ion adsorption and fast-Faradic reactions in order to store energy. These devices generally have lower energy densities compared to LIBs but have power densities that are orders of magnitude greater. Supercapacitors are typically used for back-up power or uniterruptible power sources (UPS) due to the fact that they are able to be rapidly charged and discharged. In addition, supercapacitors have life-cycles that dwarf even the most advanced LIBs. While both supercapacitors and LIBs are great for applications in their niche, they are unsuitable for applications that require both a high energy and power density such as HEVs and EVs. To that end, researchers have recently focused on a new type of electrochemical energy storage that takes the advantages of both the lithium-ion battery and the supercapacitor. The LIC uses a cathode that relies on fast adsorption and desorption of the negative electrolyte ion while the anode is an insertion-type electrode that relies on the insertion and extraction of lithium ions. This means that the overall energy density of the device depends on the cathode while the power density depends on the anode. Additionally, the life cycle of the whole device also depends on the anode because the cathode materials typically exhibit life cycles that are much greater than the anode materials.

Metal oxides play an important role in the field of energy storage due to their interesting redox reactions and potential for high energy electrochemical storage devices. Among the many metal oxides, TiO_2 is a very promising candidate for next generation electrode materials due to its low-cost, abundance in the Earth's crust, low toxicity and high stability. TiO_2 has already been used commercially in a wide range of applications from photocatalysis, paint pigments, catalyst support and UV blockers in sunscreen. Most recently, TiO_2 and its associated polymorphs has been investigated for use in LIBs and supercapacitors.

Several approaches can be made in order to improve the performance of anode materials. Fundamentally, the electrode materials can be designed with nanostructures specifically engineered in order to have fast lithium ion diffusion kinetics and high surface area in order to facilitate ion transport [21]. Another method to increase performance is to develop binder-free electrodes [9]. Traditional electrode preparation involves the addition of conductive fillers and polymeric binders. These additional materials are necessary but also decrease the volumetric energy and power density of the device. Thus, binder-free electrode preparations is an easy and direct method to improve device performance.

Herein, we report a novel binder-free composite anode material that is based on TiO_2 nanocrystals drop-casted onto a carbon cloth. The TiO_2 is synthesized using a facile 2-phase solvothermal method that produces a monodispered nanocrystalline TiO_2 that are approximately 10 nm in diameter.

5.2 Experimental

5.2.1 Materials

All chemicals used in the following work were purchased from Sigma Aldrich and was used as-is unless otherwise noted.

5.2.2 TiO$_2$ Synthesis

TiO$_2$ was synthesized using a 2-phase solvothermal method reported elsewhere. Firstly, the water phase was made by mixing 20 mL of distilled deionized water and 0.2 mL of tert-butylamine while the oil phase consists of 20 mL of toluene, 330 uL of titanium isopropoxide and 2 mL of oleic acid. The 2 separate phases are then transferred into a 100 mL steel autoclave with a Teflon liner. The autoclave is then heated to 180˚C and then left to cool to room temperature in the fume hood. The resulting oleic acid-capped TiO$_2$ is then washed with methanol and then re-dispersed in toluene. This stock solution was then diluted to the desired concentration. This reaction forms a monodispersed TiO$_2$ nanocrystals that are capped with oleic acid. The oleic acid cap serves as an emulsifier that allows the nanocrystals to be solubilized in organic solvents such as toluene. The solution of nanocrystals in toluene is stable and will not form any precipitates even if left sitting for weeks on end.

5.2.3 Carbon Cloth Preparation

Commercial carbon cloth was purchased in bulk and was cleaned using a 3-step procedure. The carbon cloth was first submerged in a solution of ethanol and then sonicated for 30 minutes then dried in a vacuum oven. This cleaning step is then repeated twice more using methanol and isopropanol. The resulting clean carbon cloth is then heat-treated at 900˚C in a tube furnace

36

under an inert Argon atmosphere. The heat treatment serves to carbonize any polymeric binders or coatings used in the manufacturing of the cloth in order to improve its conductivity. SEM was used to observe the surface of the carbon fiber cloth before and after heat treatment. It was found that the surface was not visibly altered after heat treatment. The cleaned and heat treated carbon cloth was then used in further experiments.

5.2.4 Electrode preparation

Binder free electrodes were fabricated by a simple drop casting method followed by an annealing process schematically shown in figure 21.
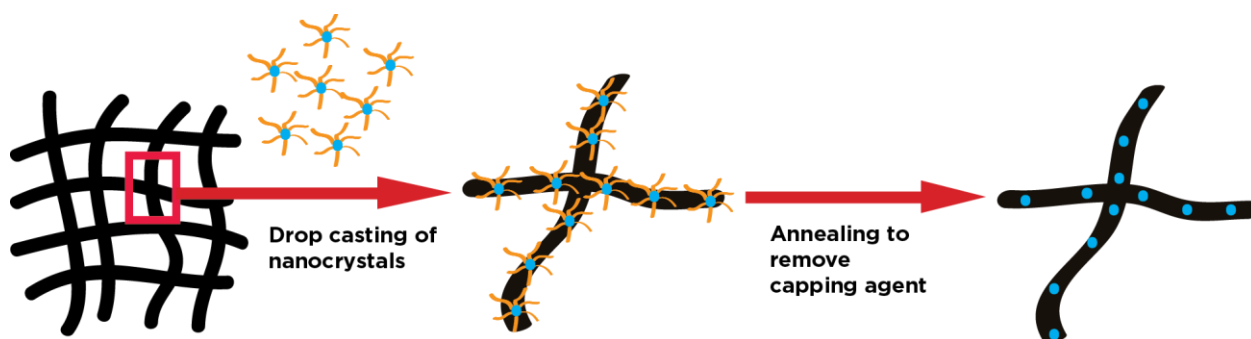
Figure 17 Schematic illustration of TiO₂/CC composite electrode with the capping removed

First, carbon cloth was cut into 12 mm circular electrodes using a commercially available electrode punch. Then, TiO_2/toluene solution was added dropwise using a pipette onto the carbon cloth until the desired loading was achieved. The resulting composite material was then annealed in a tube furnace under an air atmosphere at 450°C for 3 hours at a heating rate of 1°C/min. The electrodes were also annealed under an inert argon atmosphere at various temperatures for 3

hours at a heating rate of 1˚C/min in an effort to improve the electrical conductivity by carbonizing the oleic acid capping, as shown in figure 22.
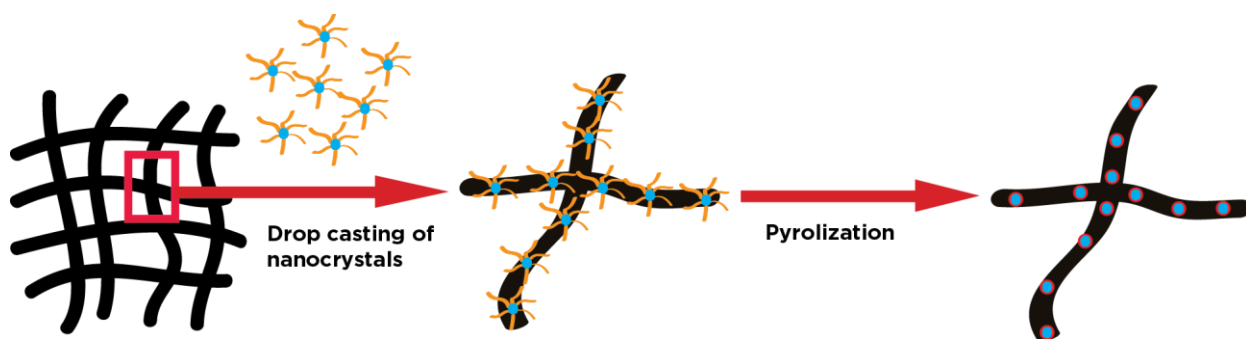
Figure 18 Schematic illustration of the TiO₂/CC electrode with a carbonized outer layer

As a comparison, electrodes were also made using the traditional slurry-based method using commercially available TiO_2 nanoparticles (Degussa P25) with an average diameter of 25 nm. In brief, the TiO_2 nanoparticles were grinded together with polyvinyldifluoride (PVDF) and conductive carbon with a ratio of 8:1:1 until a homogeneous mixture was achieved. The resulting homogeneous mixture was then suspended in n-methyl-2-pyrrolidone. The resulting suspension was then sonicated for 15 minutes and then stirred on a magnetic stir plate for 6 hours until a homogenous slurry was obtained. The slurry was then coated uniformly onto a piece of copper foil, which has been previously cleaned using ethanol, using a doctor blade and then dried in a vacuum oven to remove any excess solvents.

To demonstrate another advantage of binder-free electrode, a flexible pouch half-cell was fabricated using lithium foil as a cathode, TiO_2/CC as the anode, Cellgard 2500 as a separator and $LiPF6$ in EC/DMC was used as the electrolyte solution. The non-sensitive parts of the cell

were assembled under a normal atmosphere. The partially assembled cell was then transferred into a glovebox with a dry and inert Argon atmosphere where the lithium foil and electrolyte was assembled. Finally, the pouch cell was assembled under a vacuum to ensure good contact between the electrodes in the pouch.

5.2.5 Electrochemical Characterization

The electrochemical half-cell performance of the as prepared composite electrodes were evaluated by assembling them into CR2032 coin cells with a cellulose separator, lithium counter-electrode. The organic electrolyte used is the commonly used lithium-ion battery electrolyte which consists of 1M of LiPF6 salt dissolved in a mixture of ethyl carbonate and dimethyl carbonate. GCD was performed using a Neware battery testing station.

5.2.6 Physical Characterization

The carbon cloth, TiO_2 nanocrystals and the composite electrodes were characterized a variety of techniques. Images of the bare carbon cloth and the composite electrodes were taken using a Zeiss LEO 1530 Field-Emission SEM (FESEM) with a 10 kV accelerating voltage. No gold sputtering was done as the samples had sufficient conductivity. The average size of the TiO_2 nanocrystals capped with oleic acid were estimated using SEM as well.

The mass ratio of the oleic acid capping and the TiO_2 nanocrystals itself was determined by using TGA. The TGA was operated in air at a heating rate of 10/min.

The anatase structure of the TiO_2 crystals were confirmed using powder XRD and the crystalline size was estimated using the Scherrer equation. Raman spectroscopy was also used to confirm the presence of TiO_2.

5.3 Results and Discussion

SEM images of the TiO_2/CC composite material is shown in figure 23. Figure 23 (a) – (c) shows the surface of the composite electrode before it was annealed and (d) – (e) shows the surface of the electrode after annealing. It can be seen that the pre-annealed TiO_2 forms a uniform, polymer-esque coating on the surface of the carbon fibers. This is due to the oleic acid capping that helps mesh the TiO_2 particles seamlessly. When the electrode is annealed in air, the oleic acid capping was removed making the TiO_2 spheres stand out more as seen in the SEM images. The oleic acid helps distribute the particles uniformly on the carbon fibers which maximizes the exposed surface area of the TiO_2 nanoparticles for lithium diffusion. The small particle size ($<$ 10nm) also helps shorten the lithium-diffusion pathway by maximizing the surface area to volume ratio. This allows greater lithium-ion access to the inner structure of the TiO_2 which increases the overall energy capacity. The uniformity of the particles on the surface of the carbon fiber also ensures intimate contact between the substrate and TiO_2 which increases the number of electron conducting pathways. By doing this, the rate capabilities of the composite electrode may be enhanced, allowing for a faster charge and discharge cycle.
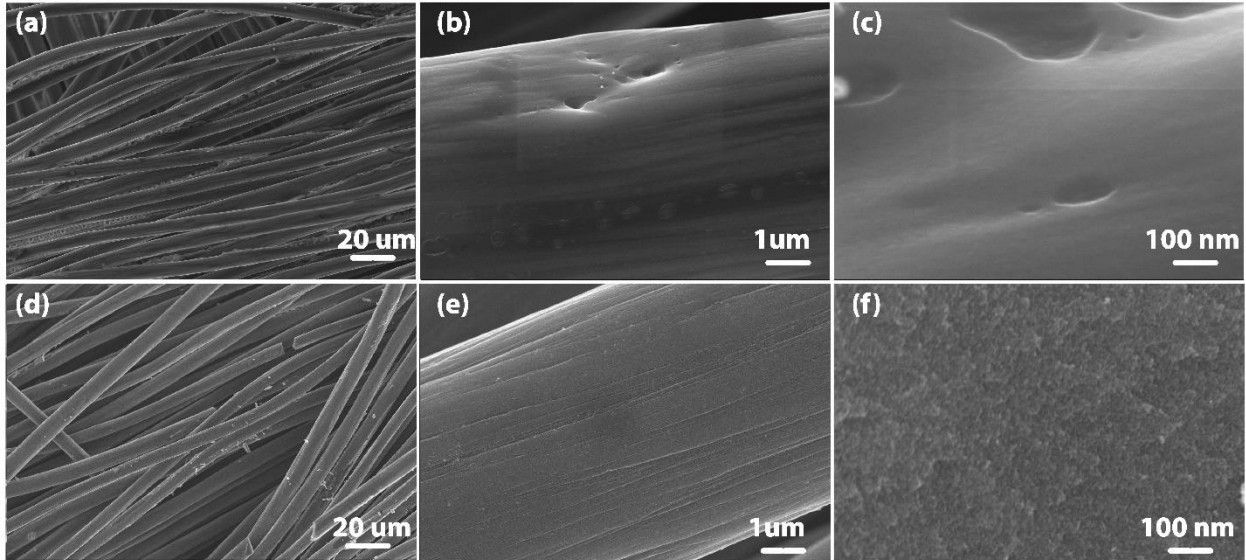
Figure 19 SEM images of TiO₂/Carbon Cloth composite at various magnifications: (a) – (c) Pre-annealing, (d)-(f) post-annealing

Figure 24 shows the raman spectrograph and x-ray diffractograms of the composite electrode. The raman spectrograph shows both the G and D bands at ~1400 cm^{-1} and ~1600 cm^{-1} which is comes from the graphitic structure found on carbonaceous materials. There is a sharp peak at ~150 cm^{-1} which is characteristic of anatase TiO$_2$ [44]. The raman spectrograph shows that there is no change in the TiO$_2$ crystal structure after the electrode is annealed as there are no shifts or additional peaks that appear in the post-anneal curve.

The XRD diffractogram mirrors the results shown by Raman spectroscopy. The XRD pattern of the plain TiO$_2$ nanocrystals matches well with that of bulk anatase TiO$_2$ (JCPDS Card No. 21-1272). The diffractogram also shows that the crystal structure remains unchanged after drop-casting and annealing to remove the oleic capping agent. Using the Scherrer equation mentioned in previous sections, the approximate crystalline domain size of the TiO$_2$ crystals can be used. The (101) peak was used for the equation and an approximate size of 10.8 nm was obtained. This

is consistent with the SEM images previously shown especially when taking account instrumentation errors.
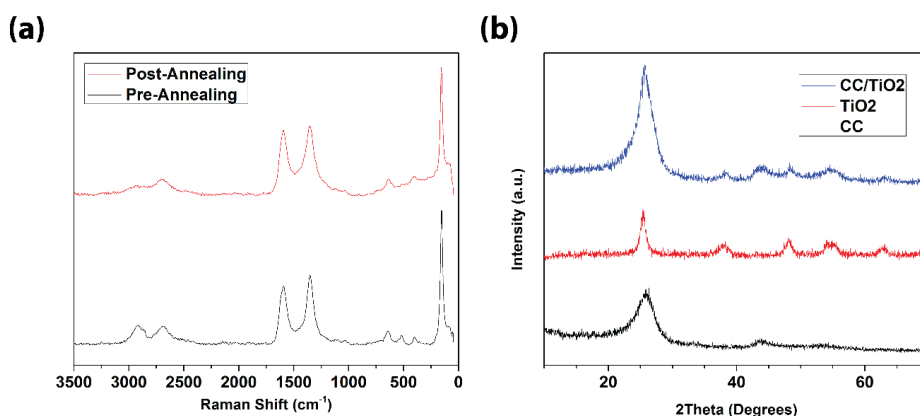
Figure 20 (a) Raman spectrograph of post- and pre-annealed electrodes, (b) X-ray diffractogram of neat carbon cloth (black), post-annealed TiO₂ particles (red), post-annealed composite electrode (blue)

Figure 25 shows the TGA curve of the TiO_2 nanocrystals. The curve shows that the nanocrystals start losing mass right away which can be attributed to the decomposition of the oleic acid capping and the evaporation of water. The mass loss continues as the temperature is further increase and the mass stabilizes once the temperature reaches $500°C$. Since the TGA is done in a normal atmosphere, it can be assumed that all of the oleic acid has combusted, leaving pure TiO_2. Thus, the composition of the TiO_2 nanocrystals was found to be 80% TiO_2 and 20% oleic acid and other organics leftover from the reaction by mass. It can also be seen on the curve that the mass slightly increases as the temperature is ramped up. This can be attributed to a drift error from the TGA machine and should not affect any of the aforementioned conclusions. The TiO_2 mass loading is important since the energy capacity of the electrode will be determined by the

quantity of TiO$_2$ deposited onto the surface of carbon cloth. Subsequent electrode loadings were adjusted to account for the 20% mass of oleic acid.
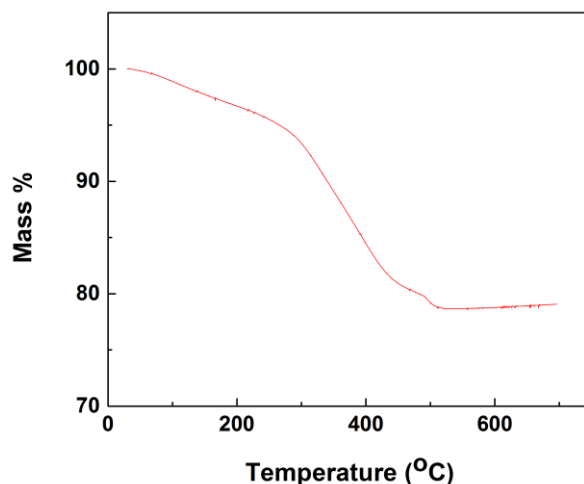
Figure 21 TGA curve of the TiO$_2$ nanocrystals

Figure 26 shows the specific capacities of the composite electrode in comparison to a slurry-based electrode. The slurry-based electrode was made using a commercially available TiO$_2$ nanoparticles that have a size of 25 nm. These nanoparticles are then mixed with other materials to form a slurry and then pasted onto a foil current collector then made into the same coin-cell form as the binder-free composite electrode. This is a similar procedure as ones used in industries to manufacture electrodes for LIBs and lithium-ion capacitors, As shown by figure 26 (b), the commercial TiO$_2$ nanoparticles have a much lower performance, topping out at 100 mAh/g at a current density of 100 mA/g. In comparison, the binder-free composite electrode have a specific discharge capacity of over 300 mAh/g at the same current density. This performance trend is similar as the current density is increased. One possible reason for this trend is the fact that the capacity is normalized by the mass loading of the electrode. This obviously favours binder-free electrodes due to the fact that only the active material, which contribute to the capacity of the

electrode, is loaded onto the current collector. In contrast, slurry-based electrodes use up to 20% by mass of non-active materials that do not contribute to the overall energy density. In addition, the presence of polymeric binders may reduce the electrical conductivity of the electrode and increase the internal contact resistance which lowers the high-rate capabilities of the electrode. Another explanation for the difference in performance is the size of the TiO_2 nanoparticles themselves. As shown in previous sections, the size of the particles is directly tied to the ability of the crystal structure to host lithium-ions. As the particles go down below 10 nm, the lithium-TiO_2 intercalation compound starts to behave like a solid solution which allows a higher density of lithium-ions to be packed, increasing the electrode's capacity [21].
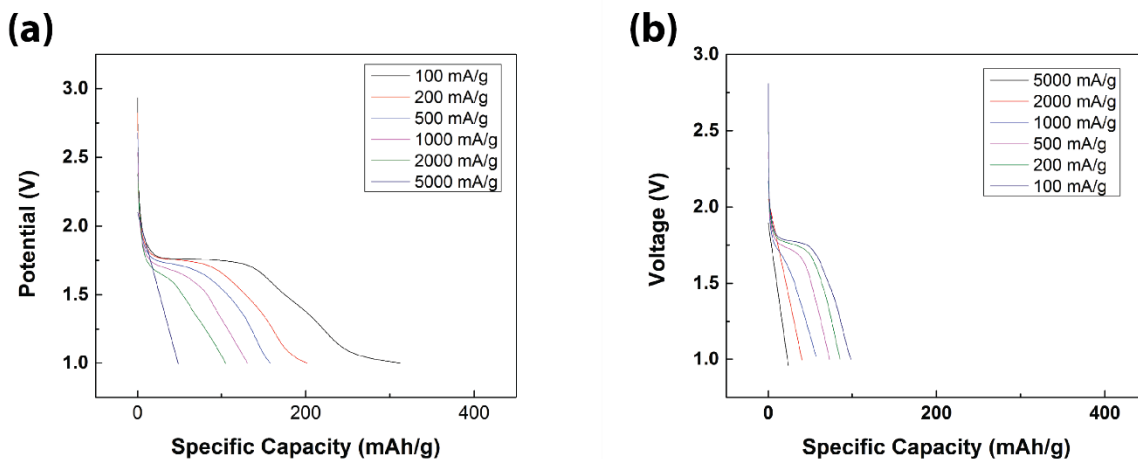
Figure 22 Capacities at different current densities for: (a) Composite, binder-free electrode (b) Traditional slurry-based electrode using commercial TiO2 nanoparticles

Figure 27 shows the effect of the TiO$_2$ solution concentration when drop casting on the capacity of the electrode. There seems to be an optimal drop casting concentration in order to maximize the capacity. As the concentration decreases, the performance of the electrode increases. This may be explained by particle aggregation on the electrode. Although the particles are able to be fully dissolved in toluene, the high concentrations might allow for aggregation once the solvent evaporates. Lower concentrations were not investigated as it would be impractical to fabricate electrodes with higher loadings. However, it can be assumed that lower solution concentrations will increase the performance by ensuring an even distribution of the particles onto the surface of the current collector.

Figure 23 Rate performance comparison between different electrodes made from various TiO$_2$ solution concentrations

The optimized drop casting concentration was then used for subsequent electrode fabrication. Figure 28 shows the galvanostatic charge and discharg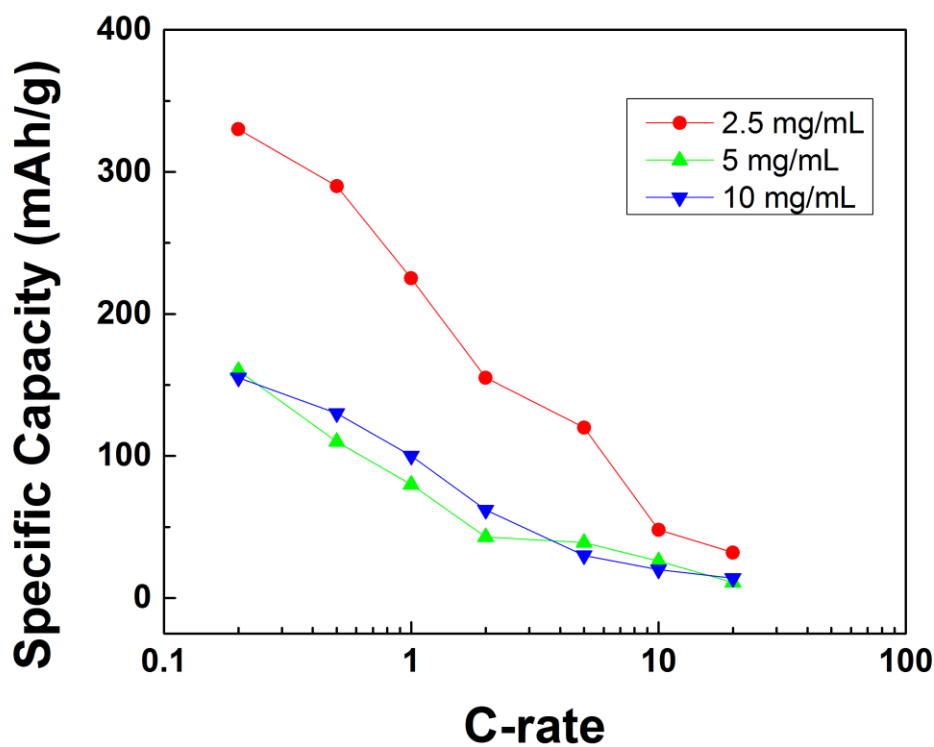e testing results. Figure 28 (a) shows the first charge and discharge capacities of the composite electrode which shows both the li-ion insertion and extraction potentials. The insertion and extraction potential is at ~1.7V and ~1.9V respectively, which matches with results shown in literature [21], [22], [42]. The capacity of TiO_2 can be broken down into diffusion- and surface-controlled regimes. The charge/discharge plateau corresponds to the diffusion-controlled capacity. In this region, the lithium ions are diffusing into the crystal structure of TiO_2 and the capacity is limited by the solid mass transport of the ions and the diffusion length. As the crystal size decreases, the capacity in this region will increase as the diffusion length of the lithium ions decrease and vice versa. The low-sloped, linear region of the charge/discharge curve correspond to the surface-controlled capacity. In this region, the lithium ions react and adsorb onto the surface/near-surface of the TiO_2 crystals and is limited by the available surface area. As the crystal size decreases, the surface-controlled region will generally also increase due to the increased surface area to volume ratio. For higher current densities, the ratio of diffusion- and surface-controlled capacity will decrease since the lithium will have less time to fully permeate the crystal structures. The charge and discharge curve will be fully linear, corresponding to a fully surface-limited capacity (similar to EDLCs), when the current density gets too high.

Figure 28 (b) shows the discharge capacities of the composite electrode at different current densities. The electrode is charged and discharged for 10 cycles at increasing current densities. Then, the current is reduced to the initial value in order to determine if any capacity is lost due to degradation of the electrode. The first discharge capacity of the electrode at 100 mA/g is around 310 mAh/g which reduces to approximately 280 mAh/g. This capacity loss can be

attributed to the formation of the SEI. Thus, the electrode can be said to have a reversible capacity of 280 mAh/g. As the current increases, the capacity drops as expected due to the aforementioned mechanisms. It can be seen that the same current densities, the charge and discharge capacity of the electrode remains relatively stable. This indicates that the structure of the electrode is not altered or degraded due to the lithium insertion and extraction. When the current is decreased back down to the initial value of 100 mA/g, the reversible capacity bounces back to the initial value of 280 mAh/g even after 70 charge and discharge cycles at various current densities. This shows that the electrode has promising stability and will be able to be cycled many times. To demonstrate the flexibility of the electrode, a pouch half-cell was made and used to power and LED as shown in figure 28 (c).
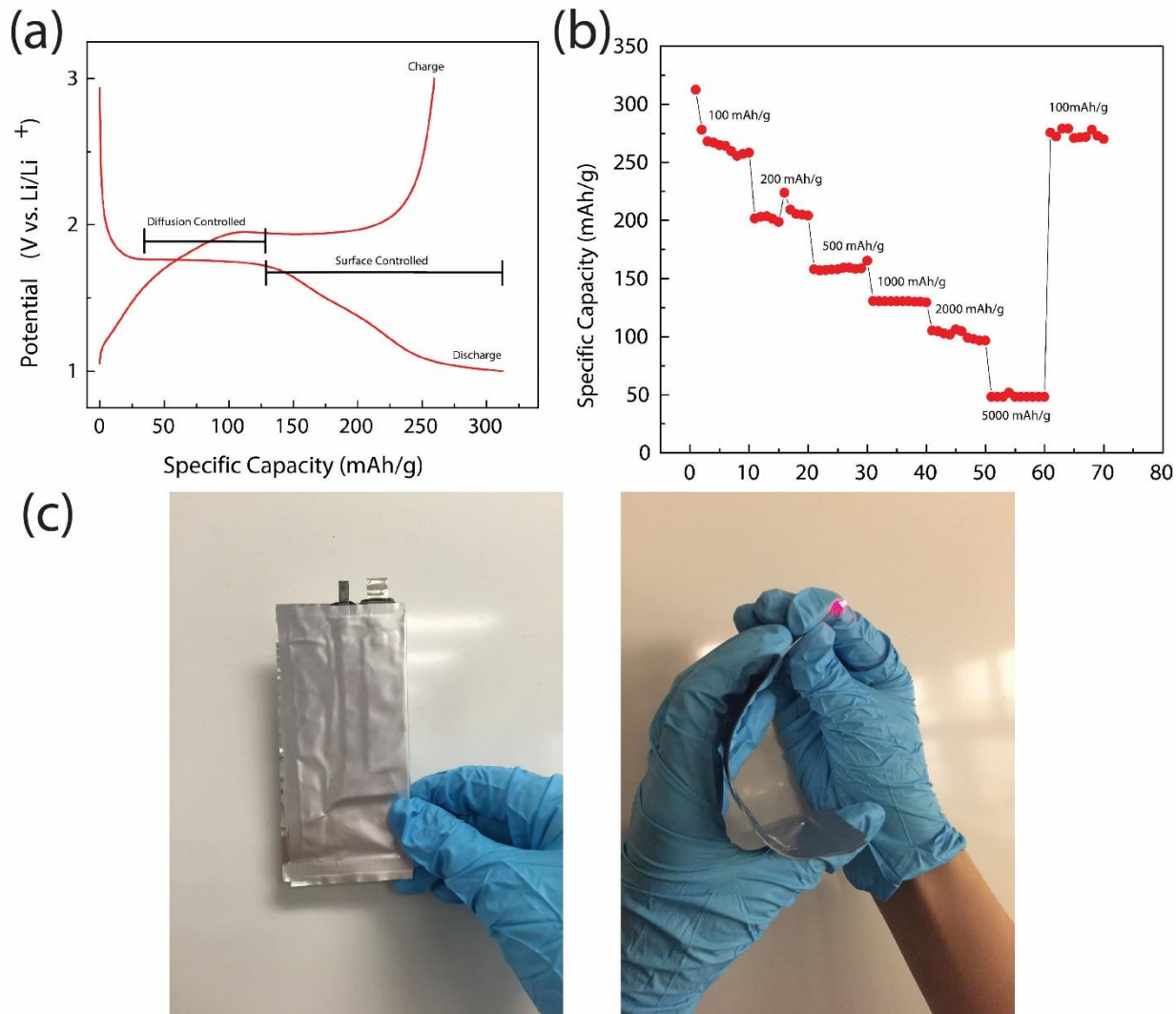
Figure 24 (a) first discharge curve of the TiO₂/CC composite, (b) rate performance of the composite electrode, (c) flexible pouch half-cell made using the composite anode

One of the simplest way to increase the high-rate performance is to increase the electrical conductivity of the electrode [16], [38]. Some other battery technologies, such as lithium iron phosphate batteries, have employed the carbon coating strategy in order to increase the conductivity. A similar strategy can be employed in the case of the TiO₂/CC composite electrodes since the TiO₂ nanocrystal synthesis process uses oleic acid as a capping agent.

48

Oleic acid is a natural fatty acid – an organic molecule with a carboxylic acid head and a long hydrocarbon chain. The oleic acid helps the TiO_2 dissolve into organic solvents by acting as a surfactant. Conveniently, the oleic acid can also be used as a carbon source to coat the TiO_2 nanocrystals. Figure 29 shows the SEM images of the composite electrodes annealed in air ((a) to (c)) and argon ((d) to (f)). The composite electrode that was annealed in air will have no oleic acid left as it has been burned away. Meanwhile, the electrode that was annealed in argon will have a carbonized oleic acid layer on the surface of the TiO_2 nanocrystals. It can be seen in figure 29 (e) that the particles are less defined when compared to figure 29 (c) due to the residual carbon that is left from the oleic acid. In order to gauge the level of carbonization, the electrodes were annealed in argon at different temperatures then made into cells and tested. Figure 30 shows the discharge capacities of the electrodes at various current densities. Note that 1C is defined as the current at which the electrode is completely discharged in 1 hour. In this case, 1C is defined at 170 mA/g which corresponds to the theoretical reversible capacity of bulk anatase TiO_2 of 170 mAh/g.
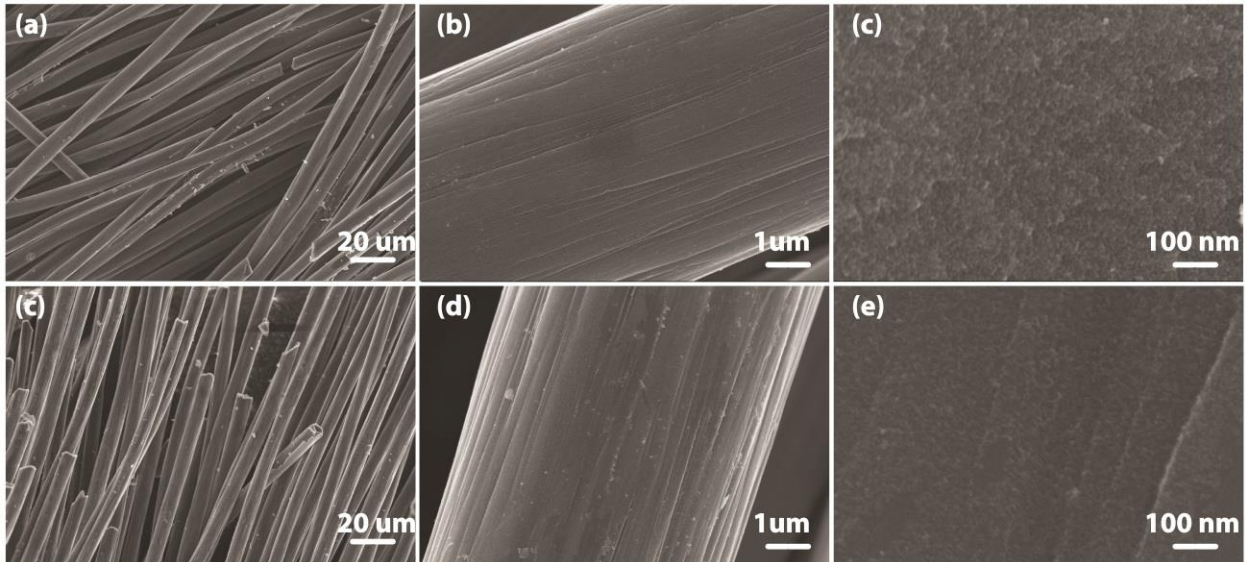
Figure 25 SEM images comparing (a)-(c) TiO2/CC electrode with removal of oleic acid and (d)-(f) composite electrode with carbonization of oleic acid

Figure 30 shows the rate performance of the carbonized composite electrodes that were annealed at different temperatures. There is a general trend of increasing performance as the annealing temperature is increased, with a maximum of around 410 mAh/g a current density fo 34 mA/g, exceeding the theoretical capacity of anatase TiO_2. The vast difference between the high and low temperatures may be explained by the presence of un-carbonized oleic acid. When argon is used during annealing at lower temperatures (400-450ºC), the thermal energy is not high enough to remove the functional groups and carbonize the oleic acid. This will affect the electrode performance since oleic acid is non-conductive. In addition, the oleic acid reduces the available surface area of the active material, forming a flat polymeric-like coating on the substrate as shown in figure 23 (c). As the temperature is increased, the carbonization of oleic acid may proceed, removing most of the functional groups on the oleic acid and leaving a conductive carbon coating on the surface as shown in figure 29 (e). This may also explain the difference between the low-current performance of the non-carbonized and carbonized

electrodes since the carbon coating may contribute to the capacity of the electrode. However, the high rate performance does not improve indicating that there are improvements to me made.
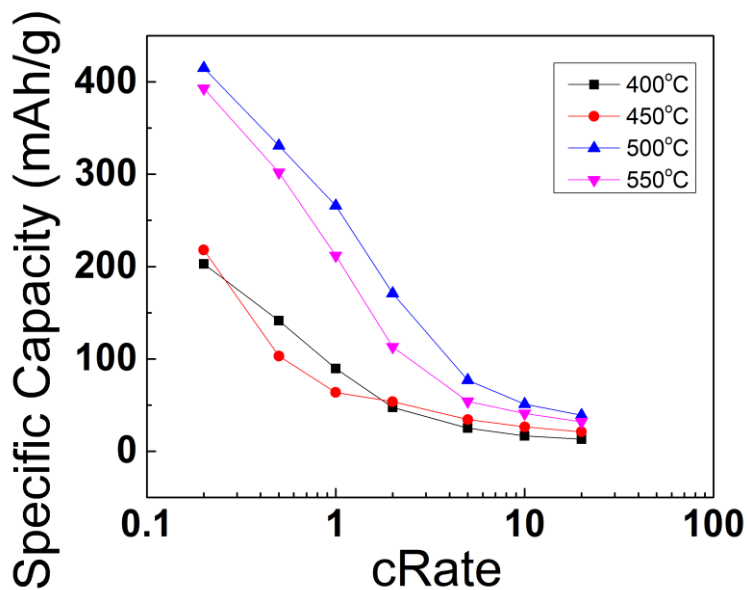

Figure 26 Rate performance comparison of TiO2/CC electrodes with carbonized oleic acid at different carbonization temperatures

6.0 Conclusions and Future Directions

LICs has a promising future as the next-generation electrochemical energy storage device for use in applications that require both high energy and power densities. However, despite being commercialized, there are a lot of ways in which it can be improved especially when the anode is concerned. TiO_2 has been shown to have excellent performance when used in LIC anodes. Introducing nanostructured TiO_2 has been shown to be an effective strategy in increasing performance. The increase in performance can be attributed to a higher available specific surface area that is characteristic of nanomaterials and also to shorter lithium-diffusion pathways during insertion and extraction. Another strategy to increase device performance is to eliminate the need for binding agents when fabricating electrodes. Herein, successful efforts have been made in order to combine both strategies to improve the performance of LIC anodes. TiO_2 nanocrystals that have sizes smaller than 10 nm were synthesized and drop casted onto carbon cloth to produce a composite electrode material. The small crystal size aids in shortening the lithium-diffusion pathway and also to increase the available surface area to the electrolyte solution. The nanocrystals were able to be easily deposited onto the carbon cloth substrate due to the oleic acid capping agent (that are able to be removed or carbonized) that helps act as a surfactant to dissolve the crystals in toluene. This ability to be completely dissolve helps in ensuring a uniform coating onto the substrate. The electrode was shown to have a reversible capacity of 315 mAh/g (oleic acid was removed) and 410 mAh/g (oleic acid was carbonized) at a current density of 100 mA/g and 34 mA/g respectively.

Although the low current performance of the electrodes were excellent, more work needs to be done to increase the high-rate performance. One approach would be to add another insertion-type electrode as a composite to increase the overall energy density. Another would be to increase the loading of the active material while still maintaining the available surface area. This can be done by changing the substrate to ones with a higher aspect ratio such as graphene or carbon nanotubes.

References

[1] S. Flandrois and B. Simon, "Carbon materials for lithium-ion rechargeable batteries," *Carbon*, vol. 37, no. 2, pp. 165–180, Feb. 1999.

[2] M. Agostini, B. Scrosati, and J. Hassoun, "An Advanced Lithium-Ion Sulfur Battery for High Energy Storage," *Adv. Energy Mater.*, p. n/a–n/a, Jun. 2015.

[3] V. Augustyn, P. Simon, and B. Dunn, "Pseudocapacitive oxide materials for high-rate electrochemical energy storage," *Energy Environ. Sci.*, vol. 7, no. 5, pp. 1597–1614, Apr. 2014.

[4] H. S. Choi and C. R. Park, "Theoretical guidelines to designing high performance energy storage device based on hybridization of lithium-ion battery and supercapacitor," *J. Power Sources*, vol. 259, pp. 1–14, Aug. 2014.

[5] M. Kim, F. Xu, J. H. Lee, C. Jung, S. M. Hong, Q. M. Zhang, and C. M. Koo, "A fast and efficient pre-doping approach to high energy density lithium-ion hybrid capacitors," *J. Mater. Chem. A*, vol. 2, no. 26, pp. 10029–10033, Jun. 2014.

[6] S. Hameer and J. L. van Niekerk, "A review of large-scale electrical energy storage," *Int. J. Energy Res.*, vol. 39, no. 9, pp. 1179–1195, Jul. 2015.

[7] S. R. Sivakkumar and A. G. Pandolfo, "Evaluation of lithium-ion capacitors assembled with pre-lithiated graphite anode and activated carbon cathode," *Electrochimica Acta*, vol. 65, pp. 280–287, Mar. 2012.

[8] J. Zhu, D. Yang, X. Rui, D. Sim, H. Yu, H. E. Hoster, P. M. Ajayan, and Q. Yan, "Facile Preparation of Ordered Porous Graphene–Metal Oxide@C Binder-Free Electrodes with High Li Storage Performance," *Small*, vol. 9, no. 20, pp. 3390–3397, Oct. 2013.

[9] Z. Chen, Y. Yuan, H. Zhou, X. Wang, Z. Gan, F. Wang, and Y. Lu, "3D Nanocomposite Architectures from Carbon-Nanotube-Threaded Nanocrystals for High-Performance Electrochemical Energy Storage," *Adv. Mater.*, vol. 26, no. 2, pp. 339–345, Jan. 2014.

[10] A. Yu, I. Roes, A. Davies, and Z. Chen, "Ultrathin, transparent, and flexible graphene films for supercapacitor application," *Appl. Phys. Lett.*, vol. 96, no. 25, p. 253105, Jun. 2010.

[11] J. Kim, W.-H. Khoh, B.-H. Wee, and J.-D. Hong, "Fabrication of flexible reduced graphene oxide–TiO2 freestanding films for supercapacitor application," *RSC Adv.*, vol. 5, no. 13, pp. 9904–9911, Jan. 2015.

[12] P. Simon and Y. Gogotsi, "Materials for electrochemical capacitors," *Nat. Mater.*, vol. 7, no. 11, pp. 845–854, Nov. 2008.

[13] G. Wang, L. Zhang, and J. Zhang, "A review of electrode materials for electrochemical supercapacitors," *Chem. Soc. Rev.*, vol. 41, no. 2, pp. 797–828, Jan. 2012.

[14] P. Simon and Y. Gogotsi, "Charge storage mechanism in nanoporous carbons and its consequence for electrical double layer capacitors," *Philos. Trans. R. Soc. Lond. Math. Phys. Eng. Sci.*, vol. 368, no. 1923, pp. 3457–3467, Jul. 2010.

[15] J. Zhang, Z. Shi, J. Wang, and J. Shi, "Composite of mesocarbon microbeads/hard carbon as anode material for lithium ion capacitor with high electrochemical performance," *J. Electroanal. Chem.*, vol. 747, pp. 20–28, Jun. 2015.

[16] J. Zhang, Z. Shi, and C. Wang, "Effect of pre-lithiation degrees of mesocarbon microbeads anode on the electrochemical performance of lithium-ion capacitors," *Electrochimica Acta*, vol. 125, pp. 22–28, Apr. 2014.

[17]   H. Park, M. Kim, F. Xu, C. Jung, S. M. Hong, and C. M. Koo, "In situ synchrotron wide-angle X-ray scattering study on rapid lithiation of graphite anode via direct contact method for Li-ion capacitors," *J. Power Sources*, vol. 283, pp. 68–73, Jun. 2015.

[18]   H. Wang and M. Yoshio, "Performance of AC/graphite capacitors at high weight ratios of AC/graphite," *J. Power Sources*, vol. 177, no. 2, pp. 681–684, Mar. 2008.

[19]   V. Aravindan, J. Gnanaraj, Y.-S. Lee, and S. Madhavi, "Insertion-Type Electrodes for Nonaqueous Li-Ion Capacitors," *Chem. Rev.*, vol. 114, no. 23, pp. 11619–11635, Dec. 2014.

[20]   M. Amereller, T. Schedlbauer, D. Moosbauer, C. Schreiner, C. Stock, F. Wudy, S. Zugmann, H. Hammer, A. Maurer, R. M. Gschwind, H.-D. Wiemhöfer, M. Winter, and H. J. Gores, "Electrolytes for lithium and lithium ion batteries: From synthesis of novel lithium borates and ionic liquids to development of novel measurement methods," *Prog. Solid State Chem.*, vol. 42, no. 4, pp. 39–56, Dec. 2014.

[21]   M. Wagemaker, W. J. H. Borghols, and F. M. Mulder, "Large Impact of Particle Size on Insertion Reactions. A Case for Anatase LixTiO2," *J. Am. Chem. Soc.*, vol. 129, no. 14, pp. 4323–4327, Apr. 2007.

[22]   Z. Yang, D. Choi, S. Kerisit, K. M. Rosso, D. Wang, J. Zhang, G. Graff, and J. Liu, "Nanostructures and lithium electrochemical reactivity of lithium titanites and titanium oxides: A review," *J. Power Sources*, vol. 192, no. 2, pp. 588–598, Jul. 2009.

[23]   D. Dambournet, I. Belharouak, and K. Amine, "Tailored Preparation Methods of TiO2 Anatase, Rutile, Brookite: Mechanism of Formation and Electrochemical Properties," *Chem. Mater.*, vol. 22, no. 3, pp. 1173–1179, Feb. 2010.

[24]   M. V. Koudriachova, N. M. Harrison, and S. W. de Leeuw, "Diffusion of Li-ions in rutile. An ab initio study," *Solid State Ion.*, vol. 157, no. 1–4, pp. 35–38, Feb. 2003.

[25]   M. V. Koudriachova, N. M. Harrison, and S. W. de Leeuw, "Effect of Diffusion on Lithium Intercalation in Titanium Dioxide," *Phys. Rev. Lett.*, vol. 86, no. 7, pp. 1275–1278, Feb. 2001.

[26]   Y.-S. Hu, L. Kienle, Y.-G. Guo, and J. Maier, "High Lithium Electroactivity of Nanometer-Sized Rutile TiO2," *Adv. Mater.*, vol. 18, no. 11, pp. 1421–1426, Jun. 2006.

[27]   M. A. Reddy, M. S. Kishore, V. Pralong, V. Caignaert, U. V. Varadaraju, and B. Raveau, "Room temperature synthesis and Li insertion into nanocrystalline rutile TiO2," *Electrochem. Commun.*, vol. 8, no. 8, pp. 1299–1303, Aug. 2006.

[28]   C. J. Howard, T. M. Sabine, and F. Dickson, "Structural and thermal parameters for rutile and anatase," *Acta Crystallogr. B*, vol. 47, no. 4, pp. 462–468, Aug. 1991.

[29]   Y. Cai, "Non-aqueous hybrid supercapacitors fabricated with mesoporous TiO2 microspheres and activated carbon electrodes with superior performance," vol. 253, no. Complete, pp. 80–89.

[30]   T. P. Feist, "The soft chemical synthesis of TiO2 (B) from layered titanates," *J. Solid State Chem.*, vol. 101, no. 2, pp. 275–295.

[31]   M. A. Reddy, V. Pralong, U. V. Varadaraju, and B. Raveau, "Crystallite Size Constraints on Lithium Insertion into Brookite TiO2," *Electrochem. Solid-State Lett.*, vol. 11, no. 8, pp. A132–A134, Aug. 2008.

[32]   M. Zukalová, M. Kalbáč, L. Kavan, I. Exnar, and M. Graetzel, "Pseudocapacitive Lithium Storage in TiO2(B)," *Chem. Mater.*, vol. 17, no. 5, pp. 1248–1255, Mar. 2005.

[33]   E. Ferg, R. J. Gummow, A. de Kock, and M. M. Thackeray, "Spinel Anodes for Lithium-Ion Batteries," *J. Electrochem. Soc.*, vol. 141, no. 11, pp. L147–L150, Nov. 1994.

[34]   T. Ohzuku, A. Ueda, and N. Yamamoto, "Zero-Strain Insertion Material of Li [Li1 / 3Ti5 / 3] O 4 for Rechargeable Lithium Cells," *J. Electrochem. Soc.*, vol. 142, no. 5, pp. 1431–1435, May 1995.

[35]   K. M. Colbow, J. R. Dahn, and R. R. Haering, "Structure and electrochemistry of the spinel oxides LiTi2O4 and Li4/3Ti5/3O4," *J. Power Sources*, vol. 26, no. 3–4 pt2, pp. 397–402, 1989.

[36]   T. Yuan, W.-T. Li, W. Zhang, Y.-S. He, C. Zhang, X.-Z. Liao, and Z.-F. Ma, "One-Pot Spray-Dried Graphene Sheets-Encapsulated Nano-Li4Ti5O12 Microspheres for a Hybrid BatCap System," *Ind. Eng. Chem. Res.*, vol. 53, no. 27, pp. 10849–10857, Jul. 2014.

[37]   R. Xue, J. Yan, L. Jiang, and B. Yi, "Fabrication of lithium titanate/graphene composites with high rate capability as electrode materials for hybrid electrochemical supercapacitors," *Mater. Chem. Phys.*, vol. 160, pp. 375–382, Jun. 2015.

[38]   X. Chen, Z. Li, L. Wei, X. Li, S. Liu, and J. Gu, "Fabrication of hierarchical cabbage-like carbonaceous materials by one-step cobalt-assisted hydrothermal carbonization of furfural," *Microporous Mesoporous Mater.*, vol. 210, pp. 149–160, Jul. 2015.

[39]   M.-S. Balogun, C. Li, Y. Zeng, M. Yu, Q. Wu, M. Wu, X. Lu, and Y. Tong, "Titanium dioxide@titanium nitride nanowires on carbon cloth with remarkable rate capability for flexible lithium-ion batteries," *J. Power Sources*, vol. 272, pp. 946–953, Dec. 2014.

[40]   L. Jiang, X. Lu, C. Xie, G. Wan, H. Zhang, and T. Youhong, "Flexible, Free-Standing TiO2–Graphene–Polypyrrole Composite Films as Electrodes for Supercapacitors," *J. Phys. Chem. C*, vol. 119, no. 8, pp. 3903–3910, Feb. 2015.

[41] J. Goldstein, *Practical Scanning Electron Microscopy: Electron and Ion Microprobe Analysis*. Springer Science & Business Media, 2012.

[42] J. Goldstein, D. E. Newbury, P. Echlin, D. C. Joy, A. D. R. Jr, C. E. Lyman, C. Fiori, and E. Lifshin, *Scanning Electron Microscopy and X-Ray Microanalysis: A Text for Biologists, Materials Scientists, and Geologists*. Springer Science & Business Media, 2012.

[43] E. Smith and G. Dent, *Modern Raman Spectroscopy: A Practical Approach*. John Wiley & Sons, 2013.

[44] T. Ohsaka, F. Izumi, and Y. Fujiki, "Raman spectrum of anatase, TiO2," *J. Raman Spectrosc.*, vol. 7, no. 6, pp. 321–324, Dec. 1978.

[45] J. Wei, J.-X. Liu, Z.-Y. Wu, Z.-L. Zhan, J. Shi, and K. Xu, "Research on the Electrochemical Performance of Rutile and Anatase Composite TiO2 Nanotube Arrays in Lithium-Ion Batteries," *J. Nanosci. Nanotechnol.*, vol. 15, no. 7, pp. 5013–5019, Jul. 2015.